JOURNAL OF COMPUTATIONAL PHYSICS **143,** 628–664 (1998)
ARTICLE NO. CP985977

Removing the Stiffness of Curvature in Computing 3-D Filaments

Thomas Y. Hou,*,[1] Isaac Klapper,†,[2] and Helen Si‡

*Applied Mathematics, California Institute of Technology, Pasadena, California 91125; †Department of Mathematical Sciences, Montana State University, Bozeman, Montana 59717; and ‡Applied Mathematics, California Institute of Technology, Pasadena, California 91125
E-mail: *hou@ama.caltech.edu, †klapper@math.montana.edu, and ‡si@ama.caltech.edu

Received September 23, 1997; revised March 10, 1998

In this paper, we present a new formulation for computing the motion of a curvature-driven 3-D filament. This new numerical method has none of the high order time step stability constraints that are usually associated with curvature regularization. This result generalizes the previous work of Hou *et al*. (1994) for 2-D fluid interfaces with surface tension. Applications to 2-D vortex sheets, 3-D motion by curvature, the Kirchhoff rod model, and nearly anti-parallel vortex filaments will be presented to demonstrate the robustness of the method. © 1998 Academic Press

1. INTRODUCTION

In this paper, we present a new formulation for computing the motion of a curvature-driven 3-D filament. This new numerical method has none of the high order time step stability constraints that are usually associated with curvature regularization. This result generalizes the previous work of Hou *et al*. [7] for 2-D fluid interfaces with surface tension. Applications to 2-D vortex sheets, 3-D motion by curvature, the Kirchhoff rod model and anti-parallel vortex filaments will be presented to demonstrate the robustness of the method.

Accurate numerical computation of the evolution of a free interface is at the heart of a large number of scientific and engineering problems. Examples include the evolution of a phase boundary in solidification, the breakup of drops in sprays, multi-fluid interfaces, and the motion of cells in the blood. In many applications, local curvature (or surface tension) has an important effect on the dynamics of interfaces. On the other hand, curvature also introduces new difficulties at the numerical level since curvature contains high order spatial derivatives

[1] Research of this author is supported in part by NSF Grant DMS-9407030 and DOE Grant DE-FGO3-89ER25073.

[2] Research of this author is supported in part by NSF Grant DMS-9704486.

0021-9991/98 $25.00

in the equations of motion for the interface. If an explicit method is used, these terms induce strong stability constraints on the time step. These stability constraints are generally time dependent and become more severe by the differential clustering of points along the interface. We refer to this time stability constraint as stiffness. This stiffness is especially difficult to remove for fluid interfaces with surface tension. Surface tension introduces stiffness to the evolution equation in a nonlinear and nonlocal manner. A straightforward implicit discretization leads to a nonlinear and nonlocal system which is difficult to invert in general.

Hou *et al*. [7] proposed to remove the stiffness of surface tension for 2-D fluid interfaces by using the small scale decomposition technique and reformulating the problem in the tangent angle and arclength metric variables. This is the so-called $\theta - L$ frame (see, e.g., [5]). This reformulation greatly improves the stability constraint. It allows us to perform well-resolved calculations for large times. Many interfacial problems that were previously not amenable are now solvable using this method.

However, this $\theta - L$ frame cannot be generalized directly to 3-D filaments since the tangent angle is not well defined. In this paper, we propose to use curvature κ as the new dynamical variable when computing 2-D and 3-D free interfaces with curvature regularization. We found that for 3-D filaments, the natural curvature and torsion variables are not suitable for computational purpose; see also [10]. The reason is that the torsion variable may be singular whenever curvature is zero. This is purely an artificial parameterization singularity. To overcome this difficulty, we propose to use generalized curvatures and the rate of rotation as the dynamical variables, $\kappa_1, \kappa_2, \omega$. These variables can be related to the natural curvature κ and torsion τ variables but also have a physical interpretation in terms of the curvature and twist of a thin nonisotropic rod. As in 2-D, the total arclength, $L(t)$, is also used as another dynamical variable. Together we obtain a new set of evolution equations for the filament. We show that by using this reformulation, we can easily remove the stiffness associated with curvature regularization.

To demonstrate the robustness of the method, we apply our method to a number of interesting applications. Our numerical study for vortex sheets with surface tension indicates that our new formulation shares the same stability property as the $\theta - L$ formulation introduced in [7]. Our numerical experiments also demonstrate convincingly that this idea works equally well for 3-D filaments calculations, such as the motion by curvature, the Kirchhoff rod model, and anti-parallel vortex filaments. The Kirchhoff rod model has received increasing interest in recent years because it can be used as a model to study the dynamics of proteins and supercoiled DNA [17]. Our numerical calculations reveal some interesting equilibrium states for the Kirchhoff rod model. With our new formulation, we can now afford to perform well-resolved and long-time computations for problems in computational geometry and computational biology. The dynamics of vortex filaments has been studied analytically and numerically over the past 30 years (see [13] for references). It has important applications involving secondary three-dimensional instability in mixing layers and boundary layers in high Reynolds number flows. Here we apply our method to study the interaction of anti-parallel vortex filament pair using a simplified model proposed by Klein *et al*. [13]. Our results compare well with those obtained in [13]. Our approach can also be applied to the case when the nonlocal term becomes important. Generalization of this idea to 3-D free surfaces has also been carried out. This will be reported elsewhere.

The organization of the rest of the paper is as follows. In Section 2, we derive the $\kappa - L$ formulation for two-dimensional interfaces, with an application to vortex sheets with surface

tension. Section 3 is devoted to 3-D filaments using the $\kappa_1 - \kappa_2 - \omega - L$ formulation. As an example of illustration, we consider the motion of a 3-D curve by its local curvature. We then apply this idea to a couple more interesting applications, the Kirchhoff rod model and anti-parallel vortex filaments in Sections 4 and 5. We discuss some practical implementation issues in Section 6. Finally, in Section 7, we present some numerical results which include vortex sheets with surface tension, motion of a 3-D curve by curvature, the Kirchhoff rod model, and anti-parallel vortex filaments.

2. THE $\kappa - L$ FORMULATION FOR 2-D INTERFACES

In this section, we derive the $\kappa - L$ method for 2-D interfaces. We first motivate the formulation for the simple model problem of motion by curvature. Then we derive the formulation for fluid interfaces and indicate how the $\kappa - L$ formulation can be used to remove the stiffness of surface tension for fluid interface problems.

2.1. *Motion by Curvature*

We motivate the $\kappa - L$ approach by considering the motion by curvature in 2-D. Let a curve Γ be given by

$$\mathbf{X}(\alpha, t) = (x(\alpha, t), y(\alpha, t)), \qquad \alpha \in [0, 2\pi], \tag{1}$$

where α parameterizes the curve. Then $\mathbf{X}$ evolves by

$$\mathbf{X}_t = U\mathbf{n}, \qquad U = \kappa, \tag{2}$$

where $\mathbf{n} = (-y_s, x_s)$ is the right-handed normal and $\kappa = x_s y_{ss} - x_{ss} y_s = (x_\alpha y_{\alpha\alpha} - x_{\alpha\alpha} y_\alpha)/s_\alpha^3$ is the signed curvature. Here s is arclength, and the s and α derivatives can be exchanged through the relation $\partial/\partial s = (1/s_\alpha)(\partial/\partial\alpha)$, where $s_\alpha = \sqrt{x_\alpha^2 + y_\alpha^2}$. We assume $\mathbf{X}$ is 2π-periodic in α. If we discretize Eq. (2) using an explicit method, this will give a time-step stability constraint in the form of $\Delta t \le C\bar{h}(t)^2$, where $\bar{h}(t)$ is the minimum grid spacing at time t. An implicit integration method, like the backward Euler or Crank–Nicholson scheme, would give a more stable discretization. But since curvature is a nonlinear function of the interface position, this would give rise to a nonlinear system for the implicit solution at the next time step.

The $\kappa - L$ approach, on the other hand, makes the application of an implicit method much easier. It consists of two steps:

(A) Formulate the evolution using the κ and s_α as the new dynamical variables.

(B) Introduce a change of frame in the parameterization of Γ so that s_α is independent of α and depends only on time. Thus, the equation for s_α becomes an ODE for L, the length of the curve Γ. This reformulation of interface motion is motivated by the $\theta - L$ frame in [5] (also see [7]).

We notice that the shape of the curve is determined solely by its normal velocity U. A tangential motion only results in a change in frame for the parameterization of the curve. Therefore, we can add a tangential motion to the dynamics without changing the interface's shape, i.e.,

$$\mathbf{X}_t = U\mathbf{n} + T\mathbf{s},$$

where $\mathbf{s} = (x_s, y_s)$ is the unit tangent vector, T is the added tangential velocity which will be determined later. To derive the evolution equations for κ and s_α, we use the Frènet equations, $\partial_s \mathbf{s} = \kappa \mathbf{n}$ and $\partial_s \mathbf{n} = -\kappa \mathbf{s}$. The evolution equations for s_α and κ are given by

$$s_{\alpha t} = T_\alpha - U\kappa s_\alpha \tag{3}$$

$$\kappa_t = \frac{1}{s_\alpha}\left(\frac{U_\alpha}{s_\alpha}\right)_\alpha + \frac{T\kappa_\alpha}{s_\alpha} + U\kappa^2. \tag{4}$$

Given s_α and κ, the position $(x(\alpha, t), y(\alpha, t))$ can be reconstructed (see Section 5). For motion by curvature, we have $U = \kappa$. The evolution in terms of κ and s_α is

$$s_{\alpha t} = T_\alpha - \kappa^2 s_\alpha \tag{5}$$

$$\kappa_t = \frac{1}{s_\alpha}\left(\frac{\kappa_\alpha}{s_\alpha}\right)_\alpha + \frac{T\kappa_\alpha}{s_\alpha} + \kappa^3. \tag{6}$$

For an explicit integration method, the stability constraint from the diffusion term is of the form

$$\Delta t < C \cdot (\bar{s_\alpha} h)^2, \tag{7}$$

where $\bar{s_\alpha} = \min_\alpha s_\alpha$, and h is the initial grid spacing in α. Therefore, the stability constraint is determined by the minimum grid spacing (i.e., $h s_\alpha \approx \Delta s$), which is time dependent and, for motion by curvature, is always decreasing.

In the reformulated system consisting of Eqs. (5) and (6), an implicit discretization becomes much easier since the highest order terms are linear. The discretization can be simplified further if s_α does not depend on α. This can be easily accomplished by choosing a special tangential velocity T to force s_α equal to its mean,

$$s_\alpha = \frac{1}{2\pi}\int_0^{2\pi} s_{\alpha'}(\alpha', t)\, d\alpha' = \frac{1}{2\pi} L(t), \tag{8}$$

where L is the length of the curve Γ. It follows from Eq. (5) that T satisfies

$$T_\alpha - \kappa^2 s_\alpha = \frac{1}{2\pi}\int_0^{2\pi} \left(T_{\alpha'} - \kappa^2 s_{\alpha'}\right) d\alpha',$$

which implies

$$T(\alpha, t) = T(0, t) + \frac{L}{2\pi}\int_0^\alpha \kappa^2\, d\alpha' - \frac{\alpha L}{(2\pi)^2}\int_0^{2\pi} \kappa^2\, d\alpha'. \tag{9}$$

Here $T(0, t)$ is simply an arbitrary change of frame which can be taken to be 0. Now since s_α just depends on time t, but not on α, the PDE for s_α is reduced to an ODE for L, and L and κ evolve by

$$L_t = -\frac{L}{2\pi}\int_0^{2\pi} \kappa^2\, d\alpha' \tag{10}$$

$$\kappa_t = \left(\frac{2\pi}{L}\right)^2 \kappa_{\alpha\alpha} + \frac{2\pi}{L} T\kappa_\alpha + \kappa^3. \tag{11}$$

Notice that because the highest order term has no spatially varying prefactor, an implicit method can be easily applied to the PDE for κ. It is sufficient to treat the leading order terms implicitly and discretize the lower order terms explicitly. Also, because the equation for L is free of stiffness, we can use an explicit method such as the Adams–Bashforth method. Then at every time step, L can be updated explicitly, and the implicit solution κ at the new time step can be obtained explicitly by using the Fourier transform.

2.2. *The Formulation for 2-D Fluid Interfaces*

In the next two subsections, we will show how to generalize the idea presented in the previous subsection to fluid interface problems. The fluid interface problem is more difficult than motion by curvature because it involves nonlocal singular integral operators. To derive an efficient implicit discretization, we also use the so-called "small scale decomposition" technique which separates the leading order contribution of a singular integral operator from the lower order contributions. Since stiffness enters only at small scales, it is enough to treat the leading order operators implicitly. For fluid interfaces, these leading order intergal operators are the Hilbert transform and its variants. They can be diagonalized using the Fourier transform. Thus we obtain an efficient implicit discretization at the same cost as an explicit method.

We consider the motion of an interface Γ given by $\mathbf{X} = (x(\alpha), y(\alpha))$, separating two inviscid, incompressible, and irrotational fluids. The density is assumed to be constant on each side of Γ. The velocity on either side of Γ is evolved according to the incompressible Euler equation

$$\mathbf{u}_{jt} + (\mathbf{u}_j \cdot \nabla)\mathbf{u}_j = -\frac{1}{\rho}\nabla(p_j + \rho_j g y), \qquad \nabla \cdot \mathbf{u}_j = 0. \tag{12}$$

Here $j = 1$ for the fluid below Γ and $j = 2$ for the fluid above, p_j is the pressure, ρ_j is the density, and gy is the gravitational potential. The boundary conditions are

$$(i)\ [\mathbf{u}]_\Gamma \cdot \mathbf{n} = 0, \qquad \text{the kinematic boundary condition,} \tag{13}$$

$$(ii)\ [p]_\Gamma = \tau\kappa, \qquad \text{the dynamic boundary condition,} \tag{14}$$

$$(iii)\ \mathbf{u}_j(x, y) \to (\pm V_\infty, 0) \text{ as } y \to \pm\infty, \qquad \text{the far field boundary condition,} \tag{15}$$

where $[\cdot]$ denotes the jump taken from above to below the interface. The velocity has a tangential discontinuity at Γ. The velocity away from Γ has the integral representation (see, e.g., [2]),

$$(u(x, y), v(x, y)) = \frac{1}{2\pi}\int \gamma(\alpha')\frac{(-(y - y(\alpha')), x - x(\alpha'))}{(x - x(\alpha'))^2 + (y - y(\alpha'))^2}\, d\alpha', \tag{16}$$

where γ is called the (unnormalized) vortex sheet strength. The true vortex sheet strength (i.e., the tangential velocity jump) is given by

$$\tilde{\gamma} = \frac{\gamma(\alpha)}{s_\alpha} = [\mathbf{u}]_\Gamma \cdot \mathbf{s}. \tag{17}$$

While there is a discontinuity in the tangential component of the velocity at Γ, the normal

component, $U(\alpha)$, is continuous and given by (16) as

$$U(\alpha) = \mathbf{W} \cdot \mathbf{n}, \tag{18}$$

where

$$\mathbf{W}(\alpha) = \frac{1}{2\pi} \text{P.V.} \int \gamma(\alpha') \frac{(-(y(\alpha) - y(\alpha')), x(\alpha) - x(\alpha'))}{(x(\alpha) - x(\alpha'))^2 + (y(\alpha) - y(\alpha'))^2} \, d\alpha'. \tag{19}$$

The P.V. in front of the integral denotes the principal value integral. This integral is called the Birkhoff–Rott integral. Using the representation (16) for the velocity, Euler's equation at the interface, and the Laplace–Young condition, the equations of motion for the interface are

$$\mathbf{X}_t = U\mathbf{n} + T\mathbf{s} \tag{20}$$

$$\gamma_t - \partial_\alpha((T - \mathbf{W} \cdot \mathbf{s})\gamma/s_\alpha) = -2A_\rho \left(s_\alpha \mathbf{W}_t \cdot \mathbf{s} + \frac{1}{8}\partial_\alpha(\gamma/s_\alpha)^2 + g y_\alpha - (T - \mathbf{W} \cdot \mathbf{s})\mathbf{W}_\alpha \cdot \mathbf{s}/s_\alpha \right) + S\kappa_\alpha. \tag{21}$$

Here $A_\rho = (\rho_1 - \rho_2)/(\rho_1 + \rho_2)$ is the Atwood ratio and S is a rescaled surface tension parameter (see [2]). In the special case of $A_\rho = 0$, i.e., $\rho_1 = \rho_2$, the evolution equation is greatly simplified. It is reduced to a vortex sheet equation (see [16]).

2.3. *The Equations of Motion Reposed*

In the previous subsection, boundary integral formulation is given for the motion of a vortex sheet in two-dimensional, inviscid fluid. Numerical stiffness arises through the presence of high order terms (i.e., high spatial derivatives) in the evolution. In this subsection, we reformulate the equations of motion using the small scale decomposition (SSD) for inertial flows. The small scale decomposition, which identifies and separates the dominant terms at small spatial scales, was first presented in [7]. The key idea is to identify the leading order contribution of certain singular operators at small spatial scales. Recall that the normal velocity U is given by Eqs. (18) and (19). Let the complex position of the interface be given by $z(\alpha, t) = x(\alpha, t) + iy(\alpha, t)$; then U can be expressed as

$$U(\alpha, t) = -\frac{1}{s_\alpha} \text{Im}\left\{ \frac{z_\alpha}{2\pi i} \text{P.V.} \int_{-\infty}^{+\infty} \frac{\gamma(\alpha', t)}{z(\alpha, t) - z(\alpha', t)} \, d\alpha' \right\}. \tag{22}$$

Note that the kernel in the Birkhoff–Rott integral can be decomposed into two terms:

$$\frac{1}{z(\alpha, t) - z(\alpha', t)} = \frac{1}{z_\alpha(\alpha - \alpha')} + \left[\frac{1}{z(\alpha, t) - z(\alpha', t)} - \frac{1}{z_\alpha(\alpha - \alpha')} \right]. \tag{23}$$

The most significant contribution comes from the first term on the right-hand side, since the bracketed term is analytic and corresponds to a smoothing operator. Therefore, we obtain the leading order behavior of U at small scales as

$$U(\alpha, t) \sim \frac{1}{2s_\alpha} \mathcal{H}[\gamma](\alpha, t), \tag{24}$$

where $\mathcal{H}$ is the Hilbert transform defined as

$$(\mathcal{H}f)(\alpha) = \frac{1}{\pi}\int_{-\infty}^{+\infty} \frac{f(\alpha')}{\alpha - \alpha'}\, d\alpha'. \tag{25}$$

Its Fourier transform is given by

$$\widehat{(\mathcal{H}f)}(k) = -i(sgn(k))\,\hat{f}(k). \tag{26}$$

The notation $f \sim g$ means that the difference between f and g is smoother than f and g. In terms of the new dynamic variables, s_α, κ, and γ, the equations of motion for the inertial vortex sheets are given by Eqs. (3), (4), and (21). Observe that the dominant term in Eq. (21) for γ_t is $S\kappa_\alpha$ at small scales. Now, substituting Eq. (24) into Eq. (4) gives

$$\kappa_t = \frac{1}{s_\alpha}\left(\frac{1}{s_\alpha}\left(\frac{1}{2s_\alpha}\mathcal{H}[\gamma]\right)_\alpha\right)_\alpha + P \tag{27}$$

$$\gamma_t = S\kappa_\alpha + Q, \tag{28}$$

where P and Q represent lower order terms at small spatial scales. This is the *small scale decomposition*. If s_α is given, the dominant small scale term is linear in κ and γ, but nonlocal by virtue of the Hilbert transform. An implicit discretization can be obtained by discretizing the leading order terms implicitly, but treating the lower order terms explicitly. However, if s_α is independent of α, the implicit solution can be obtained easily by fast Fourier transform, just as in the case of motion by curvature. By choosing a particular tangential velocity, s_α can indeed be independent of α.

2.4. *The $\kappa - L$ Formulation*

As we mentioned above, the tangential velocity T may be introduced into the dynamics without changing the shape of the interface. We can choose the particular expression for T so that s_α does not depend on α in its evolution. As in the case of motion by curvature, s_α is set to be equal to its mean, which is

$$s_\alpha = \frac{1}{2\pi}\int_0^{2\pi} s_{\alpha'}(\alpha', t)\, d\alpha' = \frac{1}{2\pi}L(t), \tag{29}$$

where L is the length of the interface. It follows from Eq. (3) that T satisfies the equation

$$\begin{aligned} T_\alpha - U\kappa s_\alpha &= \frac{1}{2\pi}\int_0^{2\pi}(T_{\alpha'} - U\kappa s_{\alpha'})\, d\alpha' \\ \Rightarrow T(\alpha, t) &= T(0, t) + \frac{L}{2\pi}\int_0^\alpha U\kappa\, d\alpha' - \frac{\alpha L}{(2\pi)^2}\int_0^{2\pi} U\kappa\, d\alpha'. \end{aligned} \tag{30}$$

$T(0, t)$ just gives an arbitrary change of frame and, for simplicity, can be taken to be 0. Thus, the expression for T is determined entirely by L, κ and U. Assume that Eq. (29) is satisfied initially, then Eq. (30) for T ensures that the constraint (29) is satisfied for all time. Now, the evolution of the interface is reformulated in terms of L and κ by

$$L_t = -\frac{L}{2\pi}\int_0^{2\pi} \kappa U\, d\alpha' \tag{31}$$

$$\kappa_t = \left(\frac{2\pi}{L}\right)^2 U_{\alpha\alpha} + \frac{2\pi}{L} T\kappa_\alpha + \kappa^2 U. \tag{32}$$

Given U, Eqs. (30), (31), and (32) give a complete formulation of the evolution problem.

The small scale decomposition for the inertial vortex sheets in the $\kappa - L$ formulation is now given as

$$\kappa_t = \frac{1}{2}\left(\frac{2\pi}{L}\right)^3 \mathcal{H}[\gamma_{\alpha\alpha}] + P \tag{33}$$

$$\gamma_t = S\kappa_\alpha + Q, \tag{34}$$

where P and Q denote the lower order terms, which do not contribute to the stiffness, and will be treated explicitly. In Fourier space, these equations are

$$\hat{\kappa}_t(k) = +i\frac{k}{2}\left(\frac{2\pi}{L}\right)^2 |k|\hat{\gamma}(k) + \hat{P}(k) \tag{35}$$

$$\hat{\gamma}_t(k) = +iSk\hat{\kappa}(k) + \hat{Q}(k), \tag{36}$$

where $\hat{P}$ and $\hat{Q}$ are the Fourier transforms of P and Q in Eqs. (33) and (34), and i is the imaginary unit. Now the implicit integration scheme can be easily applied together with an explicit discretization of Eq. (31). Since the lower order terms, P and Q, are treated explicitly, the implicit solution for κ and γ can be inverted explicitly. This gives an efficient implicit discretization of the fluid interface problem at the same cost as an explicit method. The numerical method in our computation will be discussed in Subsection 6.1.

3. THE $\kappa_1 - \kappa_2 - \omega - L$ FORMULATION FOR 3-D FILAMENTS

In this section, we generalize the $\kappa - L$ method to 3-D filaments. The formulation is more subtle for 3-D filaments since there are two normal vectors (e.g., the normal and the bi-normal vectors). It turns out that the choice of orthonormal basis has a significant impact on the computational method. In particular, the conventional Frènet frame for 3-D filaments is not suitable for computational purpose. It can give rise to an artificial parametrization singularity when curvature vanishes. To overcome this difficulty, we use a more general orthonormal basis which corresponds to the $\kappa_1 - \kappa_2 - \omega - L$ formulation for 3-D filaments.

Let us consider a space curve $\mathbf{X}(s, t)$: $[0, L] \to R^3$ where s is arc length and L is the total length of the curve. Alternatively we may parameterize $\mathbf{X}$ by a material coordinate α, i.e., $\mathbf{X}(\alpha, t)$: $[0, 2\pi] \to R^3$. The unit tangent vector along the curve $\mathbf{X}$ is given by $\mathbf{T}(s, t) = (d/ds)\mathbf{X}(s, t)$. A local description of the curve is provided by an appropriate set of coordinate axes. One such set is the Frènet triad consisting of the unit vectors $\mathbf{T}$, $\mathbf{N}$, and $\mathbf{B}$, the tangent, normal, and binormal vectors respectively. This orthonormal triad satisfies the well-known Frènet equations $\mathbf{T}_s = \kappa\mathbf{N}$, $\mathbf{N}_s = -\kappa\mathbf{T} + \tau\mathbf{B}$, $\mathbf{B}_s = -\tau\mathbf{N}$. κ is the curvature and τ is the torsion. We can now write the evolution equation for the curve in the Frènet frame,

$$\mathbf{X}_t(\alpha, t) = \bar{U}\mathbf{N} + \bar{V}\mathbf{B} + \bar{W}\mathbf{T}, \tag{37}$$

where $\bar{U}$, $\bar{V}$, and $\bar{W}$ are the normal, binormal, and tangential velocity components, respectively, each of which can depend on both α and t. In the 2-D case, we use s_α and κ as the new dynamical variables. Naturally, we would like to use s_α, κ, and τ as the new dynamical

variables for 3-D filaments. Using the Frènet equations, we can derive the evolution of the curve Γ in terms of s_α, κ, and τ as

$$s_{\alpha t} = \bar{W}_\alpha - \bar{U}\kappa s_\alpha \tag{38}$$

$$\kappa_t = \frac{1}{s_\alpha}\left(\frac{\bar{U}_\alpha}{s_\alpha}\right)_\alpha - \frac{2\tau\bar{V}_\alpha + \tau_\alpha\bar{V} - \bar{W}\kappa_\alpha}{s_\alpha} - \bar{U}(\kappa^2 - \tau^2) \tag{39}$$

$$\tau_t = \frac{1}{s_\alpha}\left(\frac{\left(\frac{\bar{V}_\alpha}{s_\alpha}\right)_\alpha}{\kappa s_\alpha}\right)_\alpha + \frac{1}{s_\alpha}\left(\frac{2\bar{U}_\alpha\tau + \bar{U}\tau_\alpha - \bar{V}\tau^2 s_\alpha}{\kappa s_\alpha}\right)_\alpha + \frac{\kappa\bar{V}_\alpha + \bar{W}\tau_\alpha}{s_\alpha} + 2\kappa\bar{U}\tau. \tag{40}$$

Consider the natural generalization of motion of a closed curve by curvature, namely, $\bar{U} = \kappa$, $\bar{V} = 0$ in Eq. (37). $\bar{W}$ can be added to the motion of equations without altering the shape of the curve. Thus Eqs. (38), (39), and (40) become

$$s_{\alpha t} = \bar{W}_\alpha - \kappa^2 s_\alpha \tag{41}$$

$$\kappa_t = \frac{1}{s_\alpha}\left(\frac{\kappa_\alpha}{s_\alpha}\right)_\alpha + \frac{\bar{W}\kappa_\alpha}{s_\alpha} - \kappa(\kappa^2 - \tau^2) \tag{42}$$

$$\tau_t = \frac{1}{s_\alpha}\left(\frac{\tau_\alpha}{s_\alpha}\right)_\alpha + 2\left(\frac{\kappa_\alpha\tau}{\kappa s_\alpha}\right)_\alpha + \frac{\bar{W}\tau_\alpha}{s_\alpha} + 2\kappa^2\tau. \tag{43}$$

Now, if s_α is given, the highest order terms in the equations for κ and τ are linear in κ and τ, respectively. Thus, an implicit integration method can be applied. Similar to the 2-D case, we can choose a special expression for $\bar{W}$ to enforce s_α to be independent of α. Then the highest order terms in Eqs. (42) and (43) do not have spatially varying prefactors. So the implicit discretization of κ and τ can be updated explicitly. The stability constraint has the form

$$\max_\alpha\left(\frac{2|\kappa_\alpha|}{\kappa s_\alpha}, \frac{|\bar{W}|}{s_\alpha}\right)\Delta t < h. \tag{44}$$

Note that the stability constraint depends on curvature. If κ becomes very small, we will get very strong stability constraints in the numerical computation. In fact, in the Frènet triad, $\mathbf{N}$, $\mathbf{B}$, and τ are only defined when the curvature does not vanish. In general $\mathbf{N}$ varies discontinuously through points where $\kappa = 0$ even for smooth curves. This would lead to the blowup of τ since τ depends on $\mathbf{N}_s$. This discontinuity in $\mathbf{N}$ through points where κ vanishes is artificial and is due to a poor choice of coordinate frame. For this reason, the Frénet frame is not a good choice for computational purposes.

Instead we propose to use a more general orthogonal basis $\mathbf{T}, \mathbf{N}_1, \mathbf{N}_2 = \mathbf{T} \times \mathbf{N}_1$ in our numerical calculation of 3-D filaments. The Frènet system is replaced by

$$\begin{aligned}\frac{d}{ds}\mathbf{T} &= \kappa_1\mathbf{N}_1 - \kappa_2\mathbf{N}_2\\ \frac{d}{ds}\mathbf{N}_1 &= -\kappa_1\mathbf{T} + \omega\mathbf{N}_2\\ \frac{d}{ds}\mathbf{N}_2 &= \kappa_2\mathbf{T} - \omega\mathbf{N}_1,\end{aligned} \tag{45}$$

where $\kappa_1 = \kappa\mathbf{N}\cdot\mathbf{N}_1$ and $\kappa_2 = -\kappa\mathbf{N}\cdot\mathbf{N}_2$.

There are natural relations between $\kappa_1, \kappa_2, \omega$ and κ, τ:

$$\kappa = \sqrt{\kappa_1^2 + \kappa_2^2} \tag{46}$$

$$\tau = \omega + \frac{\kappa_2 \kappa_{1s} - \kappa_1 \kappa_{2s}}{\kappa}. \tag{47}$$

If we make the special choice of $\omega = \tau$, then the new orthonormal basis is reduced to the Frènet triad. In this case, we have $\kappa_1 = \kappa$, $\kappa_2 = 0$.

The unit tangent vector $\mathbf{T}(s) = (d/ds)\mathbf{X}(s)$ is determined once the curve $\mathbf{X}(s)$ is known. Then we choose vectors $\mathbf{N}_1(0), \mathbf{N}_2(0)$ such that $(\mathbf{T}(0), \mathbf{N}_1(0), \mathbf{N}_2(0))$ are a set of orthonormal vectors. By choosing a smooth function for the rate of rotation, ω, and using the relations $\kappa_1 = \frac{d\mathbf{T}}{ds} \cdot \mathbf{N}_1$, $\kappa_2 = -\frac{d\mathbf{T}}{ds} \cdot \mathbf{N}_2$, we integrate the last two equations in (45) along the arc length, s, to determine $\mathbf{N}_1(s)$ and $\mathbf{N}_2(s)$. Notice that the first equation in (45) is automatically satisfied since we have used it to construct κ_1 and κ_2. Also, the orthogonality of these three vectors $\mathbf{T}(s), \mathbf{N}_1(s)$, and $\mathbf{N}_2(s)$ can be shown by using Eqs. (45). Thus we obtain a smooth orthonormal basis set $(\mathbf{T}(s), \mathbf{N}_1(s), \mathbf{N}_2(s))$. Clearly, this orthonormal basis is smooth as long as the curvature is smooth, even though the curvature may vanish at some points.

Now we rewrite the evolution equation for the curve in our newly chosen orthonormal basis $(\mathbf{T}, \mathbf{N}_1, \mathbf{N}_2)$:

$$\mathbf{X}_t(\alpha, t) = U\mathbf{N}_1 + V\mathbf{N}_2 + W\mathbf{T}.$$

Since we have relationships between $\mathbf{N}, \mathbf{B}$ and $\mathbf{N}_1, \mathbf{N}_2$, namely

$$\begin{aligned} \kappa\mathbf{N} &= \kappa_1\mathbf{N}_1 - \kappa_2\mathbf{N}_2 \\ \kappa\mathbf{B} &= \kappa_2\mathbf{N}_1 + \kappa_1\mathbf{N}_2, \end{aligned} \tag{48}$$

it is straightforward to determine the relationships between U, V, W and $\bar{U}, \bar{V}, \bar{W}$.

The fact that $\mathbf{X}$ has continuous second order derivatives in space and time implies that the cross derivatives of α and t commute. To carry out the computations associated with this relationship it is convenient to write the time derivatives of the basis $\mathbf{T}, \mathbf{N}_1, \mathbf{N}_2$ as

$$\mathbf{T}_t = \Lambda_F \times \mathbf{T}, \qquad \mathbf{N}_{1t} = \Lambda_F \times \mathbf{N}_1, \qquad \mathbf{N}_{2t} = \Lambda_F \times \mathbf{N}_2, \tag{49}$$

where $\Lambda_F(\alpha, t) = \lambda_1\mathbf{N}_1 + \lambda_2\mathbf{N}_2 + \lambda_3\mathbf{T}$ is the rotation vector whose components $\lambda_1, \lambda_2, \lambda_3$ are related to U, V, W and hence $\kappa_1, \kappa_2, \omega$,

$$\begin{aligned} \lambda_1 &= -\frac{V_\alpha}{s_\alpha} - U\omega + W\kappa_2 \\ \lambda_2 &= \frac{U_\alpha}{s_\alpha} - V\omega + W\kappa_1, \end{aligned} \tag{50}$$

and λ_3 will be determined later. It can be shown (also see [8]) that the equations of motion for $s_\alpha, \kappa_1, \kappa_2, \omega$ in terms of U, V, W take the form

$$s_{\alpha t} = W_\alpha + (V\kappa_2 - U\kappa_1)s_\alpha \tag{51}$$

$$\kappa_{1t} = \frac{1}{s_\alpha}\left(\frac{U_\alpha}{s_\alpha}\right)_\alpha - \frac{2\omega V_\alpha + \omega_\alpha V - W\kappa_{1\alpha}}{s_\alpha} - U\omega^2 + \kappa_1(U\kappa_1 - V\kappa_2) + \omega\kappa_2 W - \lambda_3\kappa_2 \tag{52}$$

$$\kappa_{2t} = -\frac{1}{s_\alpha}\left(\frac{V_\alpha}{s_\alpha}\right)_\alpha - \frac{2\omega U_\alpha + \omega_\alpha U - W\kappa_{2\alpha}}{s_\alpha} + V\omega^2 + \kappa_2(U\kappa_1 - V\kappa_2) - \omega\kappa_1 W - \lambda_3\kappa_1 \tag{53}$$

$$\omega_t = \frac{\kappa_1 V_\alpha + \kappa_2 U_\alpha - \omega W_\alpha}{s_\alpha} + 2\omega(U\kappa_1 - V\kappa_2) + \frac{\lambda_{3\alpha}}{s_\alpha}. \tag{54}$$

As a final remark, note that we now have four functions s, κ_1, κ_2, and ω to describe a curve in R^3. ω measures the twist rate of the $\mathbf{N}_1$–$\mathbf{N}_2$ plane around $\mathbf{T}$, and may (e.g., the Kirchhoff rod model) or may not (e.g., motion by curvature) have physical significance.

As in the 2-D case, we can choose a tangential velocity W to force s_α to be everywhere equal to its mean,

$$s_\alpha = \frac{1}{2\pi}\int_0^{2\pi} s_{\alpha'}(\alpha', t)\, d\alpha' = \frac{1}{2\pi}L(t), \tag{55}$$

where L is the length of the curve Γ. Specifically

$$W_\alpha - (U\kappa_1 - V\kappa_2)s_\alpha = \frac{1}{2\pi}\int_0^{2\pi}(W_{\alpha'} - (U\kappa_1 - V\kappa_2))s_{\alpha'}\, d\alpha'$$

$$\Rightarrow W(\alpha, t) = \frac{L}{2\pi}\int_0^{\alpha}(U\kappa_1 - V\kappa_2)\, d\alpha - \frac{\alpha L}{(2\pi)^2}\int_0^{2\pi}(U\kappa_1 - V\kappa_2)\, d\alpha'. \tag{56}$$

Now since s_α depends only on t and not α, the PDE for s_α reduces to an ODE for L. Equations for L and $\kappa_1, \kappa_2, \omega$ then reduce to

$$L_t = -\frac{L}{2\pi}\int_0^{2\pi}(U\kappa_1 - V\kappa_2)\, d\alpha' \tag{57}$$

$$\kappa_{1t} = \left(\frac{2\pi}{L}\right)^2 U_{\alpha\alpha} - \frac{2\pi}{L}(2\omega V_\alpha + \omega_\alpha V - W\kappa_{1\alpha}) - U\omega^3 + \kappa_1(U\kappa_1 - V\kappa_2) + \omega\kappa_2 W - \lambda_3\kappa_2 \tag{58}$$

$$\kappa_{2t} = -\left(\frac{2\pi}{L}\right)^2 V_{\alpha\alpha} - \frac{2\pi}{L}(2\omega U\alpha + \omega_\alpha U - W\kappa_{2\alpha}) + V\omega^2 + \kappa_2(U\kappa_1 - V\kappa_2) - \omega\kappa_1 W - \lambda_3\kappa_1 \tag{59}$$

$$\omega_t = \frac{2\pi}{L}(\kappa_1 V_\alpha + \kappa_2 U_\alpha - \omega W_\alpha) + 2\omega(U\kappa_1 - V\kappa_2) + \frac{2\pi}{L}\lambda_{3\alpha}. \tag{60}$$

We now show that for motion by curvature this reformulation leads to efficient implicit discretization. To obtain the velocity in this new basis, we project the original equation $\mathbf{X}_t = \kappa\mathbf{N}$ into the new orthonormal basis. Using the relations between $\mathbf{N}$ and $\mathbf{N}_1, \mathbf{N}_2$, we have $U = \kappa_1$ and $V = -\kappa_2$. Simply substitute U, V into Eqs. (57)–(60) and take λ_3 to be 0 (see Subsection 6.3); we then derive the formulation in terms of $\kappa_1, \kappa_2, \omega$ and L as

$$L_t = -\frac{L}{2\pi}\int_0^{2\pi}\left(\kappa_1^2 + \kappa_2^2\right) d\alpha' \tag{61}$$

$$\kappa_{1t} = \left(\frac{2\pi}{L}\right)^2 \kappa_{1\alpha\alpha} + \frac{2\pi}{L}(2\omega\kappa_{2\alpha} + \omega_\alpha\kappa_2 + W\kappa_{1\alpha}) + \kappa_1\left(\kappa_1^2 + \kappa_2^2 - \omega^2\right) + \omega\kappa_2 W \tag{62}$$

$$\kappa_{2t} = \left(\frac{2\pi}{L}\right)^2 \kappa_{2\alpha\alpha} - \frac{2\pi}{L}(2\omega\kappa_{1\alpha} - \omega_\alpha\kappa_1 + W\kappa_{2\alpha}) + \kappa_2\left(\kappa_1^2 + \kappa_2^2 - \omega_2\right) - \omega\kappa_1 W \tag{63}$$

$$\omega_t = \frac{2\pi}{L}(\kappa_2\kappa_{1\alpha} - \kappa_1\kappa_{2\alpha}). \tag{64}$$

As in the 2-D case, L and ω can be updated using an explicit integration method. The highest order terms in Eqs. (58) and (59) do not have spatially varying prefactors. We can invert the implicit discretization for the diffusion terms in the κ_1 and κ_2 equations efficiently.

4. APPLICATION TO THE KIRCHHOFF ROD MODEL

We now apply our method to the physically interesting problem of the Kirchhoff rod. The study of elastic rods is the subject of continued scientific and mathematical interest. Applications of the dynamics of rods and filaments include the dynamics of proteins and supercoiled DNA [17], writhing instability in fibers and cables [19], three-dimensional scroll waves [18], magnetic flux tubes, and the formation of sunspots [14], etc. Under some simplifying assumptions, the motion of an elastic rod filament can be well described by a one-dimensional system of equations. One such set of equations, the Kirchhoff rod equations [9], can be constructed as follows [6]. The rod is represented by its center line $\mathbf{X}(s,t)\colon [0,L] \to R^3$ and twist (defined below) $\omega(s,t)\colon [0,L] \to R$. Here s is arc length and L is the length of the rod. For simplicity we assume that the cross section of the filament is always circular with constant radius in space. Define a reference ribbon by a pair of curves $(\mathbf{X}, \mathbf{X} + \epsilon\mathbf{N}_1)$ where $\mathbf{N}_1(s,t)\colon [0,L] \to R^3$ is a unit vector field such that $\mathbf{N}_1 \cdot \mathbf{T} = 0$ ($\mathbf{T}$ is the unit tangent vector along the curve $\mathbf{X}$) and ϵ is the width of the ribbon. The twist ω (with respect to the reference ribbon $(\mathbf{X}, \mathbf{X} + \epsilon\mathbf{N}_1)$) is defined to be the rotation rate of $\mathbf{N}_1$ around $\mathbf{T}$ moving along $\mathbf{X}$; i.e., $\omega(s,t) = (\mathbf{N}_1(s,t) \times (d/ds)\mathbf{N}_1(s,t)) \cdot \mathbf{T}$. The Frènet triad is a particular choice of ribbon which corresponds to choosing $\mathbf{N}_1 = \mathbf{N}$. Recall that $\mathbf{N}$ has the same direction as $(d/ds)\mathbf{T}(s,t)$. More typically $\mathbf{N}_1$ might point in the direction of one of the principle axes of the cross section of the rod. The equations of motion can be written as

$$\frac{d^2}{dt^2}\mathbf{X} = \frac{d}{ds}\mathbf{F} - \eta_1\frac{d}{dt}\mathbf{X} + \mathbf{g} \tag{65}$$

$$\frac{d}{ds}\mathbf{M} = \mathbf{F} \times \mathbf{T} + \ddot{\theta}|_{\mathbf{x}}\mathbf{T} + \mathbf{W}_1 + \eta_2(\dot{\theta}|_{\mathbf{x}} + \mathbf{W}_2) + \mathbf{H} \tag{66}$$

$$\mathbf{M} = \Gamma^{-1}\kappa\mathbf{B} + \omega\mathbf{T}, \tag{67}$$

where $\mathbf{g}$ contains the other external forces such as gravity, contact force, etc. Γ and η_i measure respectively the relative energetic importance of twist and flexure and the relative time scales of viscosity and inertia. The rod shearing terms $\mathbf{W}_1$ and $\mathbf{W}_2$ are set to be 0 and Γ to be 1.

We rewrite the velocity of $\mathbf{X}$ in terms of the ribbon basis as

$$\mathbf{X}_t(\alpha, t) = U\mathbf{N}_1 + V\mathbf{N}_2 + W\mathbf{T},$$

where $\mathbf{N}_2 = \mathbf{T} \times \mathbf{N}_1$. To compute the main force $\mathbf{F}$, we decompose it into the local orthonormal ribbon basis:

$$\mathbf{F} = F_1\mathbf{N}_1 + F_2\mathbf{N}_2 + F_T\mathbf{T}.$$

The normal and bi-normal components of $\mathbf{F}$ can be determined immediately from Eqs. (66) and (67), that is, $F_1 = -\kappa_{1s}$ and $F_2 = \kappa_{2s}$. The determination of the tangential force $F_T = F \cdot \mathbf{T}$ is more subtle. We will derive it later. Using Eqs. (45), (49), (65), (66), and (67) we obtain the evolution equations for κ_1, κ_2, ω, and s_α as

$$s_{\alpha t} = W_\alpha - (U\kappa_1 - V\kappa_2)s_\alpha \tag{68}$$

$$\kappa_{1t} = \frac{1}{s_\alpha}\left(\frac{U_\alpha}{s_\alpha}\right)_\alpha - \frac{2\omega V_\alpha + \omega_\alpha V - W\kappa_{1\alpha}}{s_\alpha} - U\omega^2 + \kappa_1(U\kappa_1 - V\kappa_2) + \omega\kappa_2 W - \lambda_2\kappa_2 \tag{69}$$

$$U_t = -\frac{1}{s_\alpha}\left(\frac{\kappa_{1\alpha}}{s_\alpha}\right)_\alpha - \frac{\omega\kappa_{2\alpha}}{s_\alpha} + F_T\kappa_1 - W\lambda_2 + V\lambda_3 - \eta_1 U + g_1 \tag{70}$$

$$\kappa_{2t} = -\frac{1}{s_\alpha}\left(\frac{V_\alpha}{s_\alpha}\right)_\alpha - \frac{2\omega U_\alpha + \omega_\alpha U - W\kappa_{2\alpha}}{s_\alpha} + V\omega^2 + \kappa_2(U\kappa_1 - V\kappa_2) - \omega\kappa_1 W - \lambda_2\kappa_1 \tag{71}$$

$$V_t = \frac{1}{s_\alpha}\left(\frac{\kappa_{2\alpha}}{s_\alpha}\right)_\alpha - \frac{\omega\kappa_{1\alpha}}{s_\alpha} - F_T\kappa_2 + W\lambda_1 - U\lambda_3 - \eta_1 V + g_2 \tag{72}$$

$$\omega_t = \frac{\lambda_{3\alpha}}{s_\alpha} + \frac{\kappa_1 V\alpha + \kappa_2 U\alpha}{s_\alpha} + 2\omega(U\kappa_1 - V\kappa_2) - \omega\frac{W_\alpha}{s_\alpha} \tag{73}$$

$$\lambda_{3t} = \frac{\omega_\alpha}{s_\alpha} - \eta_2\frac{\lambda_3}{s_\alpha}, \tag{74}$$

where $g_1 = \mathbf{g} \cdot \mathbf{N}_1$ and $g_2 = \mathbf{g} \cdot \mathbf{N}_2$.

Equation (74) is derived from Eqs. (66) and (67). To see this, we observe that Eqs. (66) and (67) give

$$\omega_\alpha = \ddot{\theta}|_{\mathbf{X}} s_\alpha + \eta_2\dot{\theta}|_{\mathbf{X}}, \tag{75}$$

where $\dot{\theta}|_{\mathbf{x}}$ refers to $\dot{\theta}$ at a fixed filament position $\mathbf{X}$ (see [11]) (Here a dot denotes $\partial/\partial t$). If we hold $\mathbf{X}$ steady and allow twisting, we have $\mathbf{N}_{1t} = \lambda_3(\alpha, t)\mathbf{T} \times \mathbf{N}_1$. Over an element of the filament from $\mathbf{X}(\alpha)$ to $\mathbf{X}(\alpha + \Delta\alpha)$,

$$\frac{d}{dt}\Delta\theta = \lambda_3(\alpha + \Delta\alpha, t) - \lambda_3(\alpha, t),$$

where $\theta = \int^{s(\alpha)} \omega\, ds = \int^{\alpha} s_\alpha\omega\, d\alpha$ is the angle of rotation of the reference ribbon at $\mathbf{X}(\alpha, \mathbf{t})$. Thus when $\mathbf{X}$ is fixed, $\dot{\theta}|_{\mathbf{X}} = \lambda_3$, and $\ddot{\theta}|_{\mathbf{X}} = \dot{\lambda}_3$. Substituting these relations to Eq. (75) gives Eq. (74).

Now we are going to determine the tension $F_T = F \cdot \mathbf{T}$. From $\frac{\partial \mathbf{X}}{\partial \alpha} = s_\alpha \mathbf{T}$, we get

$$\begin{aligned}\frac{\partial \mathbf{X}}{\partial \alpha} \cdot \frac{\partial \dot{\mathbf{X}}}{\partial \alpha} &= s_\alpha \mathbf{T} \cdot (s_{\alpha t}\mathbf{T} + s_\alpha \mathbf{T}_t) \\ &= s_\alpha s_{\alpha t} = r s_\alpha^2, \end{aligned} \tag{76}$$

provided that the rod has prescribed extension rate $r(\alpha, t)$, i.e., $s_{\alpha t} = r(\alpha, t)s_\alpha$, which is true by our choice of W from Eq. (56). Differentiating this equation with respect to time t, we get

$$\begin{aligned}\frac{\partial \mathbf{X}}{\partial \alpha} \cdot \frac{\partial \ddot{\mathbf{X}}}{\partial \alpha} &= -\frac{\partial \dot{\mathbf{X}}}{\partial \alpha} \cdot \frac{\partial \dot{\mathbf{X}}}{\partial \alpha} + \dot{r} s_\alpha^2 + 2 r s_\alpha s_{\alpha t} \\ &= s_\alpha^2 \left(r^2 + \dot{r} - |\mathbf{T}_t|^2\right). \end{aligned} \tag{77}$$

From Eq. (49), we get $|\mathbf{T}_t| = \sqrt{\lambda_1^2 + \lambda_2^2}$. Furthermore, we have

$$\begin{aligned}\frac{\partial \mathbf{X}}{\partial \alpha} \cdot \frac{\partial \ddot{\mathbf{X}}}{\partial \alpha} &= s_\alpha \mathbf{T} \cdot \frac{\partial}{\partial \alpha} \ddot{\mathbf{X}} \\ &= s_\alpha \mathbf{T} \cdot \frac{\partial}{\partial \alpha} \left(\frac{d\mathbf{F}}{ds} - \eta \frac{d\mathbf{X}}{dt} + \mathbf{g} \right) \\ &= s_\alpha^2 \mathbf{T} \cdot (\mathbf{F}_{ss} + \mathbf{g}_s). \end{aligned} \tag{78}$$

Thus F_T satisfies

$$\begin{aligned}\frac{d^2}{ds^2} F_T - \left(\kappa_1^2 + \kappa_2^2\right) F_T = {} & 2F_{1s}\kappa_1 - 2F_{2s}\kappa_2 + F_1 \kappa_{1s} - F_2 \kappa_{2s} - \omega(F_1 \kappa_2 + F_2 \kappa_1) \\ & + r^2 + \dot{r} - \left(\lambda_1^2 + \lambda_2^2\right) + \kappa_1 g_1 - \kappa_2 g_2 - g_{ts}, \end{aligned} \tag{79}$$

with $F_1 = -\kappa_{1s}$, $F_2 = \kappa_{2s}$ and $g_t = \mathbf{g} \cdot \mathbf{T}$. The right-hand side of the equation for F_T depends only on known qualities and hence the tension is determined with the appropriate periodic boundary conditions for closed filaments.

We now summarize the small scale decomposition in the κ_1, κ_2 and ω formulae as

$$\begin{aligned}\kappa_{1t} &\sim \left(\frac{2\pi}{L}\right)^2 U_{\alpha\alpha} + P_1 \\ U_t &\sim -\left(\frac{2\pi}{L}\right)^2 \kappa_{1\alpha\alpha} + Q_1 \\ \kappa_{2t} &\sim -\left(\frac{2\pi}{L}\right)^2 V_{\alpha\alpha} + P_2 \\ V_t &\sim \left(\frac{2\pi}{L}\right)^2 \kappa_{2\alpha\alpha} + Q_2, \end{aligned}$$

with $\omega_t \sim \frac{2\pi}{L}\lambda_{3\alpha} + P_3$ and $\lambda_{3t} \sim \frac{2\pi}{L}\omega_\alpha + Q_3$, where P_i and Q_i, $i = 1, 2, 3$ are the lower order terms. The highest order terms in the equations for κ_1, κ_2, U, V, ω, and λ_3 now appear linearly. After updating L explicitly, it is a straightforward exercise to apply an implicit integration method to these equations.

5. APPLICATION TO NEARLY PARALLEL VORTEX FILAMENTS

Another interesting problem we consider is a nearly parallel pair of vortex filaments. Vortex filaments with large strength and narrow cross section are prominent fluid mechanical structures in mixed layers, boundary layers, and trailing wakes. It is interesting to study the interaction of nearly parallel and anti-parallel vortex filaments in high Reynolds number flows. An ensemble of vortex filaments interacts via the three-dimensional Biot–Savart integrals for the induced velocities on the filament centerlines. The induced motion of each filament consists of self- and foreign-induced velocity contributions. It has been shown by Callegari and Ting [3] and Klein and Majda [12] that the geometrical evolution of the filaments in the regime considered obeys the propagation law

$$\frac{\partial \mathbf{X}_i}{\partial t} = \left(\ln\left(\frac{1}{\delta}\right) + C_i\right)\frac{\Gamma_i}{4\pi}(\kappa\mathbf{B})_i + Q_i^f + Q_i^{\text{outer}}. \tag{80}$$

The first term points in the direction of the local binormal vector $\mathbf{B}_i$, and via the expression $\ln(\frac{1}{\delta}) + C_i$ describes the influence of the vortex core structure on the filament motion. Here $\delta \ll 1$ relates to the small effective core sizes and C_i is a quadratically nonlinear functional of the detailed core vorticity distribution of the ith filament (see [3] and [12]). Q_i^f is the filament motion due to nonlocal self-stretching [12] and the foreign-induced velocity Q_i^{outer} has been analyzed in [13]. Klein *et al*. derived simplified equations for a pair of interacting vortex filaments in [13],

$$\frac{\partial \mathbf{X}_i}{\partial t} = \Gamma_i(\kappa\mathbf{B})_i + 2t_0 \times \Gamma_j \frac{\mathbf{X}_i - \mathbf{X}_j}{|\mathbf{X}_i - \mathbf{X}_j|^2}, \tag{81}$$

where $t_0 = (0, 0, 1)$ and $i,\ j = 1, 2$. These simplified equations retain the important physical effects of linearized local self-induction and nonlinear potential vortex interaction among filaments but neglect other nonlocal effects of self-stretching and mutual induction. Now we apply our method to a nearly parallel vortex filament pair using the equations above. Notice that $\kappa\mathbf{B} = \kappa_2\mathbf{N}_1 + \kappa_1\mathbf{N}_2$. Using Eqs. (57)–(60), it is easy to derive the formulation in terms of $\kappa_{1i}, \kappa_{2i}, \omega_i$, and L_i and the small scale decomposition in the κ_{1i}, κ_{2i} formulae is

$$\kappa_{1it} \sim \Gamma_i \left(\frac{2\pi}{L_i}\right)^2 \kappa_{2i\alpha\alpha} + P_i$$

$$\kappa_{2it} \sim -\Gamma_i \left(\frac{2\pi}{L_i}\right)^2 \kappa_{1i\alpha\alpha} + Q_i,$$

where P_i and Q_i are the lower order terms, $i = 1, 2$. As before, the implicit solutions are easily obtained by the fast Fourier transform.

6. SOME IMPLEMENTATION ISSUES

This section is devoted to addressing a few practical implementation issues. This includes the question of what implicit discretization scheme we will use, the reconstruction of the interface from the curvature variable, and the choice of orthogonal basis in the Kirchhoff rod model.

6.1. *Time-Stepping Considerations*

The time integration scheme we used in this paper is a fourth order multi-step implicit/explicit scheme studied in [1] by Ascher *et al*. This is one of the better high order implicit/explicit schemes to use in the sense that it has a large stability region. Consider a time-dependent PDE in which the spatial derivatives have been discretized by either central differences or by pseudo-spectral methods. This gives rise to a large system of ODEs in time which typically has the form

$$\frac{du}{dt} = f(u) + \nu g(u), \tag{82}$$

where g is a linear operator containing high order derivatives and $f(u)$ is a nonlinear function which we do not want to integrate implicitly in time. To avoid using excessively small time steps, we would like to treat the $\nu g(u)$ implicitly while treating the nonlinear terms $f(u)$ explicitly. Typically $f(u)$ involves only first order derivatives from the convective terms, so the stiffness induced from the nonlinear term is not as severe as that from the linear operator $g(u)$.

The fourth order implicit/explicit scheme considered by Ascher *et al*. is given as

$$\begin{aligned}&\frac{1}{\Delta t}\left(\frac{25}{12}u^{n+1} - 4u^n + 3u^{n-1} - \frac{4}{3}u^{n-2} + \frac{1}{4}u^{n-3}\right)\\ &\quad = 4f(u^n) - 6f(u^{n-1}) + 4f(u^{n-2}) - f(u^{n-3}) + \nu g(u^{n+1}).\end{aligned} \tag{83}$$

In this paper, we simply apply this fourth order implicit/explicit scheme to our problems. For example, we use this scheme in the inertial vortex sheet problem

$$\kappa_t = \frac{1}{s_\alpha}\left(\frac{1}{s_\alpha}\left(\frac{1}{2s_\alpha}\mathcal{H}[\gamma]\right)_\alpha\right)_\alpha + P \tag{84}$$

$$\gamma_t = S\kappa_\alpha + Q, \tag{85}$$

where P and Q represent the lower order terms. We obtain the following time discrete system:

$$\begin{aligned}&\frac{1}{\Delta t}\left(\frac{25}{12}\kappa^{n+1} - 4\kappa^n + 3\kappa^{n-1} - \frac{4}{3}\kappa^{n-2} + \frac{1}{4}\kappa^{n-3}\right)\\ &\quad = \frac{1}{s_\alpha}\left(\frac{1}{s_\alpha}\left(\frac{1}{2s_\alpha}\mathcal{H}[\gamma^{n+1}]\right)_\alpha\right)_\alpha + 4P^n - 6P^{n-1} + 4P^{n-2} - P^{n-3}\end{aligned}$$

and

$$\begin{aligned}&\frac{1}{\Delta t}\left(\frac{25}{12}\gamma^{n+1} - 4\gamma^n + 3\gamma^{n-1} - \frac{4}{3}\gamma^{n-2} + \frac{1}{4}\gamma^{n-3}\right)\\ &\quad = S\kappa_\alpha^{n+1} + 4Q^n - 6Q^{n-1} + 4Q^{n-2} - Q^{n-3}\end{aligned}$$

Then with our special choice of the tangential velocity, T, s_α is independent of α, and we can solve for κ^{n+1} and γ^{n+1} explicitly using the fast Fourier transform.

6.2. *Reconstruction of the Interface from Curvature*

In our paper, the construction of the initial equal arc length parameterization is the same as in [7]. We will not repeat the details here. On the other hand, it is important to discuss the reconstruction of the 2-D interface (x, y) from (L, κ), and the 3-D filament (x, y, z) from $(L, \kappa_1, \kappa_2, \omega)$.

One natural way to reconstruct (x, y) from curvature is to integrate the Frènet equations along the interface. This will generate the tangent vector $\mathbf{T}$. We can then integrate the tangent vector along the interface to obtain the interface position. This involves two numerical integrations for each time step, and we need to keep track of two initial conditions at the beginning point of the interface. An alterative is to use the evolution equation for the interface. Recall that Γ evolves according to $\mathbf{X}_t = U\mathbf{n} + T\mathbf{s}$. We can reconstruct (x, y) through integration of these original equations. In the inertial vortex sheets problem, we know that

$$U(\alpha, t) \sim \frac{1}{2s_\alpha}\mathcal{H}[\gamma](\alpha, t),$$

so we get

$$\mathbf{X}_t = \frac{1}{2s_\alpha}\mathcal{H}[\gamma]\mathbf{n} + P, \tag{86}$$

where P includes the lower order terms. In the computation, we treat $(1/2s_\alpha)\mathcal{H}[\gamma]$ implicitly and all the other terms explicitly. However, due to the numerical error, the points on the curve are no longer equally distributed (i.e., s_α is not exactly $L/(2\pi)$ everywhere). This makes Eq. (86) incompatible with Eqs. (27) and (28). This difficulty is overcome by redistributing (x, y). For example, we can make use of the formula

$$\mathbf{X}_\alpha = \frac{L}{2\pi}\mathbf{T}, \tag{87}$$

where $\mathbf{T} = \mathbf{X}_\alpha/|\mathbf{X}_\alpha|$.

We denote the solution of Eq. (86) by $\bar{\mathbf{X}}$. Then integrate the equation

$$\mathbf{X}_\alpha = \frac{L}{2\pi|\mathbf{X}_\alpha|}\bar{\mathbf{X}}_\alpha \tag{88}$$

with respect to α to get $\mathbf{X}$ for the new time step. Of course, in the absence of numerical errors, the coefficient in front of $\bar{\mathbf{X}}_\alpha$ should be 1. We have considered other ways of redistribution, but we have found that this approach gave the best performance numerically. This method of reconstruction using the original evolution equation for $\mathbf{X}$ also applies to 3-D surfaces.

In the case of 3-D filaments, a space curve Γ evolves according to $\mathbf{X}_t = \bar{U}\mathbf{N} + \bar{V}\mathbf{B} + \bar{W}\mathbf{T}$, where $\mathbf{X} = (x(\alpha, t), y(\alpha, t), z(\alpha, t))$. If we simply reconstruct (x, y, z) by integrating these three equations, we will get a stability constraint of the form $\Delta t \le Ch^2$, since $\mathbf{N}$ involves a second derivative of $\mathbf{X}$. So, we try to reconstruct $\mathbf{X}$ using the first approach we mentioned earlier. First, we integrate Eqs. (45) to get the tangential vector $\mathbf{T}$, then we integrate Eq. (87) to get $\mathbf{X}$. By doing this, we can still have a stability constraint of the form $\Delta t \le Ch$.

6.3. *Contact Force in the Kirchhoff Rod Model*

In practice, a contact force $\mathbf{g}$ is added to Eq. (65) to avoid self-crossing of the filament. The contact force becomes important when the rod deforms in such a manner that points

separated by large differences in arc length become close to one another in space. The contact force can be modeled by the integral formula

$$\mathbf{g}(s) = -\int M(s,\sigma)\frac{U'(|r(s)-r(\sigma)|)}{|r(s)-r(\sigma)|}[r(s)-r(\sigma)]\,d\sigma, \tag{89}$$

where U is a self-potential generating a central force between pairs of points along the rod, and M is a mollifier leading to total energy and corresponding, for example, to a nonzero radius of the rod. In our example, we take the potential U to be proportional to $|r(s)-r(\sigma)|^{-9}$.

Another point we should stress is that in the case of motion by curvature, we simply take λ_3 to be 0, which makes the formulation much easier. But this cannot be done in the case of the Kirchhoff rod model. This is because in the case of motion by curvature, we are only concerned with the shape of the curve Γ, which is determined by the tangential vector. Therefore we can choose a particular $\mathbf{N}_1$ and $\mathbf{N}_2$ by taking λ_3 to be 0. In the Kirchhoff rod model, we do not just study a space curve. Instead, we study a rod with some thickness. Here the twist ω is important in the evolution of the rod and in fact depends on λ_3.

7. NUMERICAL RESULTS

In this section, the results of numerical simulations are presented for several 2-D and 3-D problems. All of these simulations use the appropriate small scale decomposition, together with the associated numerical methods discussed in the previous sections. In subsections 7.1 and 7.2, we consider motion by curvature and motion by $\kappa - \langle\kappa\rangle$ in two dimensions. These tests demonstrate that our method has only a linear stability constraint. Subsection 7.3 presents the motion of inertial vortex sheets which has been well studied by Hou *et al*. in [7]. We demonstrate that our numerical method shares a stability property similar to that of the equal arc length/tangent angle formulation. We can compute very close to the time when a pinching singularity is formed. A comparison of the stability constraint between these two methods will be given. In Subsection 7.4, we compute the motion by curvature in three dimensions. The result is consistent with our findings for 2-D interfaces. Again, our method has only a linear stability constraint. Comparison with straightforward explicit method in (x, y, z) coordinates shows that our method allows a time step 3200 times larger than that of the corresponding explicit discretization for $N = 512$. Motions for the Kirchhoff rod model and anti-parallel vortex filaments are presented in subsection 7.5 and 7.6, respectively. The results match very well with the existing results [10, 13] and no stiffness was observed in our computation.

7.1. *Motion by Curvature in 2-D*

In the next two subsections, we perform several numerical tests on motion by curvature in 2-D to demonstrate the effectiveness of our method. These tests all demonstrate that our reformulated implicit method has only a linear stability constraint, i.e., Δt is of the same order of the spacial mesh size. This linear stability constraint is expected since we treat the convection terms explicitly. From our stability analysis for the convection equation, we can see a dependence of the CFL condition on the maximum curvature. This is also verified numerically.

We consider a plane curve Γ evolving according to

$$\mathbf{X}_t = \kappa\mathbf{n}. \tag{90}$$

In our numerical calculations, we use the length of the curve and the curvature as our dynamic variables. They evolve by Eqs. (10) and (11). The reconstruction of the position of the curve is done by directly integrating the equation $\mathbf{X}_t = \kappa \mathbf{n} + T\mathbf{s}$, where T is of the form given in Eq. (9).

In our first example, we choose the initial curve as $\mathbf{X} = (\alpha + 0.2\cos(4\pi\alpha), 0.5\sin(2\pi\alpha))$, $0 \le \alpha \le 1$. We graph the position of the curve at various times. In Fig. 1, we show the continued evolution of the curve from $t = 0.0$ to $t = 0.08$. There are $N = 128$ mesh points in the unit interval with time step $\Delta t = 0.00025$.

In fact, Δt can be increased as time progresses. We list the maximum time steps that can be used at various times in Fig. 2.

The reason Δt is chosen to be so small initially is that the stability constraint is of the form

$$\max_{\alpha} |\bar{T}| \Delta t < C \cdot Lh, \tag{91}$$

from Eqs. (10) and (11). Here $\bar{T} = \int_0^\alpha (\kappa^2)\, d\alpha' - \alpha \int_0^1 (\kappa^2)\, d\alpha'$. Thus Δt is still related to the magnitude of curvature through T. We print out the curvature of this curve in Fig. 3. The maximum curvature of this curve is around 130. Since the initially curvature is large along some part of the curve, the time step has to be small to satisfy the stability constraint. We see that this periodic curve moves faster where it has bigger curvature and it relaxes to a straight line with increasing time. When we increase the number of points in the calculation, we do see the time step decreases linearly.

We next consider the initial curve $\mathbf{X} = (\alpha + 0.1\sin(2\pi\alpha), 0.5\cos(2\pi\alpha))$, $0 \le \alpha \le 1$, evolving according to Eq. (90). The maximum curvature of this initial curve is around 143. We graph the position of the curve at various times. In Fig. 4 we show the continued evolution of the curve from $t = 0.0$ to $t = 0.08$. $N = 128$ mesh points were used and the time

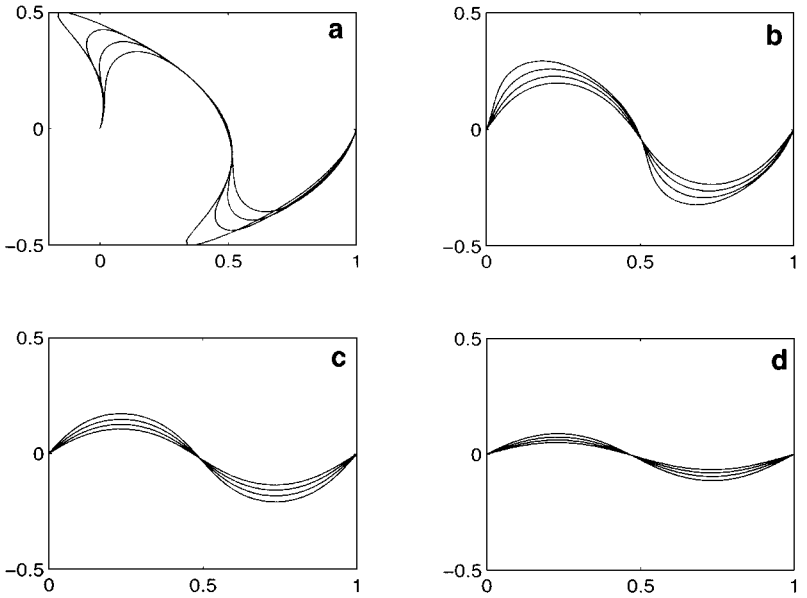

FIG. 1. Motion by curvature, initial sin curve: $N = 128$, $\Delta t = 0.00025$; curve portrayed every 0.005: (a) 0 to 0.02; (b) 0.02 to 0.04; (c) 0.04 to 0.06; (d) 0.06 to 0.08.

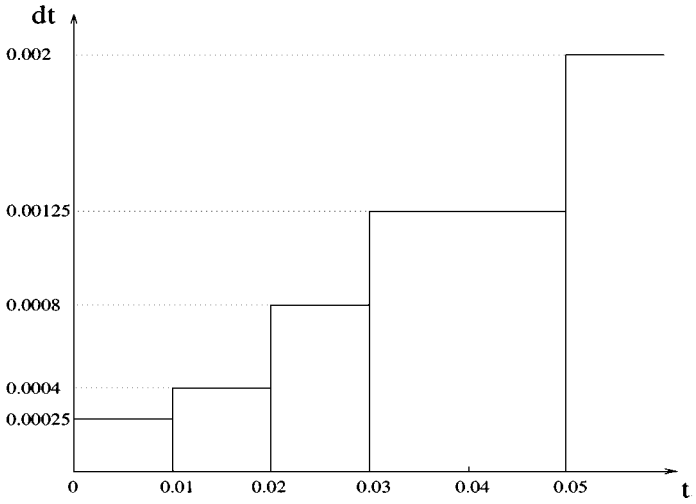

FIG. 2. Maximum time steps at various times.

step $\Delta t = 0.00005$. This periodic curve relaxes quickly to a straight line as time increases. We list the maximum time steps that can be used at various times in Fig. 5.

We also consider the evolution of the initial closed curve

$$\mathbf{X} = (1 + 0.4\sin(10\pi\alpha))(\cos(2\pi\alpha), \sin(2\pi\alpha)), \qquad 0 \le \alpha \le 1.$$

according to Eq. (90). With $N = 256$ mesh points, and time step $\Delta t = 0.001$, we show in Fig. 6 the continued evolution of the curve from $t = 0.0$ to $t = 0.2$. The plots show that this star-shaped curve quickly relaxes to a circle.

7.2. *Motion by $\kappa - \langle\kappa\rangle$ in 2-D*

We consider the initial curve $\mathbf{X} = (-2\sin(2\pi\alpha), \cos(2\pi\alpha))$ evolving according to

$$\mathbf{X}_t = (\kappa - \langle\kappa\rangle)\mathbf{n}. \tag{92}$$

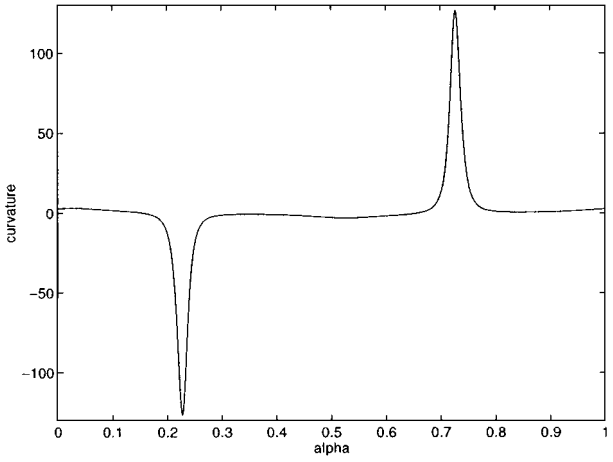

FIG. 3. Curvature of the initial sin curve.

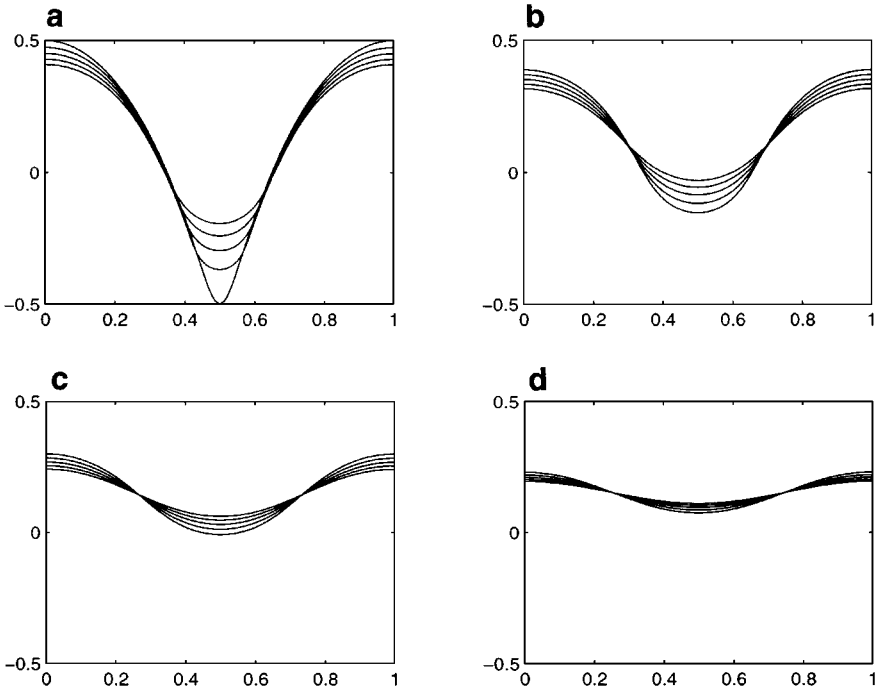

FIG. 4. Motion by curvature: $N = 128$, $\Delta t = 0.00005$; curve portrayed every 0.004: (a) 0 to 0.02; (b) 0.02 to 0.04; (c) 0.04 to 0.06; (d) 0.06 to 0.08.

Here $\langle \kappa \rangle$ is the mean of κ, i.e., $\int_0^1 \kappa \, d\alpha$. With $N = 256$ mesh points and $\Delta t = 0.005$, we show the continued evolution from $t = 0.0$ to $t = 2.0$ in Fig. 7. We see that a circle is the equilibrium state for this ellipse under the motion by $\kappa - \langle \kappa \rangle$.

We also compute the same initial curve evolving according to Eq. (90). We use $N = 256$ mesh points and $\Delta t = 0.0025$ and show the evolution from $t = 0.0$ to $t = 1.0$ in Fig. 8. Here we see that the ellipse shrinks to a point under Eq. (90).

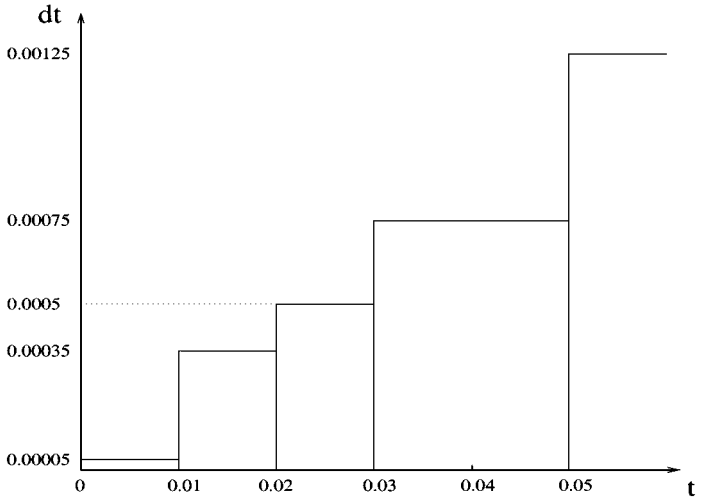

FIG. 5. Maximum time steps at various times.

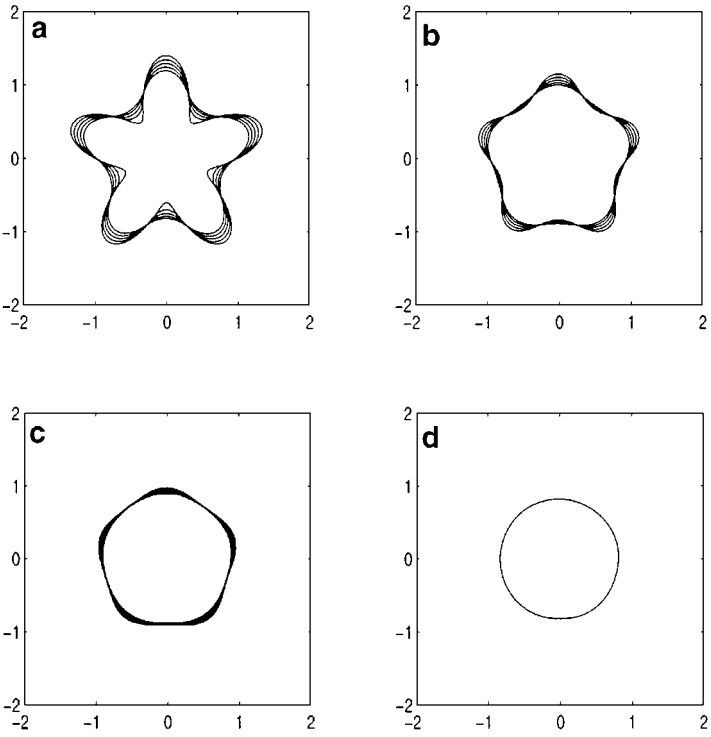

FIG. 6. Motion by curvature, star-shaped curve: $N = 256$, $\Delta t = 0.001$; curve portrayed every 0.01: (a) 0 to 0.05; (b) 0.05 to 0.1; (c) 0.1 to 0.15; (d) 0.2.

To test the dependence of Δt on the magnitude of curvature and the spatial mesh size, h, we perform a series of resolution studies for three examples. These examples give the same shapes of curves, but with increasing curvature by a constant factor, 2. In the first example, the initial curve is given by $\mathbf{X1} = (-4\sin(2\pi\alpha), 2\cos(2\pi\alpha))$. It evolves according to Eqs. (90)

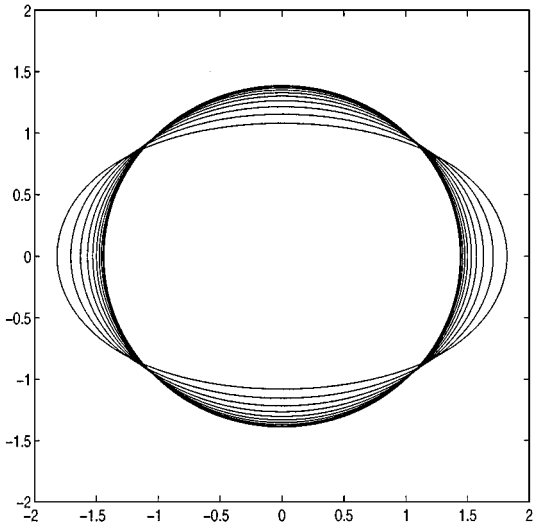

FIG. 7. $N = 256$, $\Delta t = 0.005$, $t = 0.0, 2.0(0.2)$.

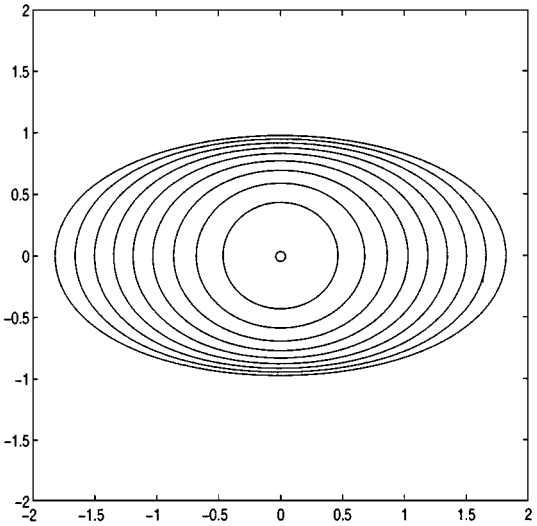

FIG. 8. $N = 256$, $\Delta t = 0.0025$, $t = 0.0, 1.0(0.1)$.

and (92). In the following table the largest possible time steps that give stable discretizations are shown.

No. of points	$U = \kappa$	$U = \kappa - \langle\kappa\rangle$
128	0.02	0.025
256	0.01	0.0125
512	0.005	0.00625

Using Eq. (90), we only calculate until $t = 4.0$, at which time the curve essentially becomes a point.

In the second example, we scale the initial curve of the first example by a factor of 2, i.e., $\mathbf{X2} = (-2\sin(2\pi\alpha), \cos(2\pi\alpha))$. We evolve it by the same equations, Eqs. (90) and (92). The largest possible time steps that give stable discretizations are given below.

No. of points	$U = \kappa$	$U = \kappa - \langle\kappa\rangle$
128	0.005	0.0075
256	0.0025	0.005
512	0.00125	0.0025

Using Eq. (90), we only calculate until $t = 1.0$ before it is essentially a point.

In the third example, we scale the initial curve of the first example by a factor of 4, i.e., $\mathbf{X3} = (-\sin(2\pi\alpha), 0.5\cos(2\pi\alpha))$, and evolve it by the same equations. Again we list below the largest possible time steps that give stable discretizations.

No. of points	$U = \kappa$	$U = \kappa - \langle\kappa\rangle$
128	0.002	0.002
256	0.001	0.001
512	0.0005	0.0005

Using Eq. (90), it will essentially be a point after $t = 0.25$.

Basically the curvature of **X3** is two times the curvature of **X2** and four times the curvature of **X1**. From Eqs. (31) and (32), the stability constraint is of the form

$$\max_{\alpha} |\bar{T}| \Delta t < CLh, \tag{93}$$

under the motion by κ or $\kappa - \langle \kappa \rangle$. Here $\bar{T} = \int_0^\alpha (U\kappa)\, d\alpha' - \alpha \int_0^1 (U\kappa)\, d\alpha'$. Since $\bar{T}$ is proportional to κ^2, the time step constraint for **X3** is approximately four times smaller than that for **X2**. Similarly the time step constraint of **X2** is approximately four times smaller than that for **X1**. This is exactly what we observed from the numerical calculations.

The above calculations all demonstrate that our numerical method is free of severe time step constraint. The time step is proportional to the space grid size in all these calculations. In fact, the particle grid spacing is decreasing in almost all the cases since the curve shrinks to a point. Without using our implicit discretization, the method would have become unstable very early on.

7.3. *Inertial Vortex Sheets*

Next, we apply our reformulated implicit scheme to the inertial vortex sheet problem with surface tension. This problem has been well studied by Hou *et al*. in [7] using the $\theta - L$ formulation. Significant improvement on stability constraint was observed over conventional explicit discretization, e.g., the fourth order Runge–Kutta method. It is natural for us to compare the performance of these two reformulated methods. Our numerical experiments indicate that these two formulations give the same stability constraint. This is also explained analytically in this subsection. This is an important and encouraging comparison, because our reformulation can be applied to 3-D problems.

In order to compare our methods with the $\theta - L$ frame presented by Hou *et al*. in [7], we examine the long-time evolution of inertial vortex sheets with surface tension. We use the same initial condition as in [7],

$$\begin{aligned} &x(\alpha, 0) = \alpha + 0.01 \sin 2\pi\alpha, \qquad y(\alpha, 0) = -0.01 \sin 2\pi\alpha, \\ &\gamma(\alpha, 0) = 1.0, \end{aligned} \tag{94}$$

and choose $S = 0.005$ as in their calculation. In Fig. 9, a time sequence of interface positions is given, starting from the initial condition. Also we plot the vortex sheet strength γ and the curvature κ at various times in Figs. 10 and 11, respectively. The calculation uses $N = 1024$ and $\Delta t = 1.25 \times 10^{-4}$. We also compare directly our numerical solutions with those obtained by the $\theta - L$ frame presented in [7]. We find that the $\theta - L$ frame and the $\kappa - L$ frame give us essentially the same numerical result. Also we have checked the stability constraint using these two formulations. We find that using the same number of points, the largest possible time steps that give stable discretizations are of the same order for the two methods. This can also be explained analytically. Using the $\theta - L$ frame (assume that $\alpha \in [0, 2\pi]$), the equations of motion are given by

$$L_t = -\int_0^{2\pi} \theta_{\alpha'} U\, d\alpha' \tag{95}$$

$$\theta_t = \left(\frac{2\pi}{L}\right)(U_\alpha + \theta_\alpha T) \tag{96}$$

$$\gamma_t = \frac{2\pi}{L} S\theta_{\alpha\alpha} + \partial_\alpha((T - \mathbf{W} \cdot \hat{s})\gamma / s_\alpha), \tag{97}$$

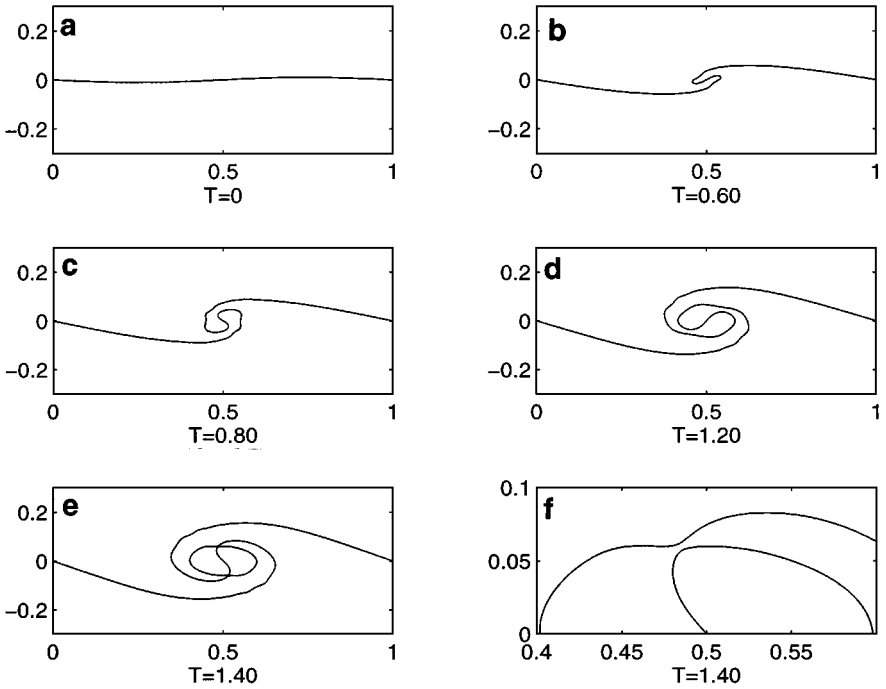

FIG. 9. Inertial vortex sheets, sequence of interface positions: $S = 0.005$, $N = 1024$, $\Delta t = 1.25 \times 10^{-4}$: (a) $t = 0$; (b) $t = 0.60$; (c) $t = 0.80$; (d) $t = 1.20$; (e) $t = 1.40$; (f) close-up of top pinching region, $t = 1.40$.

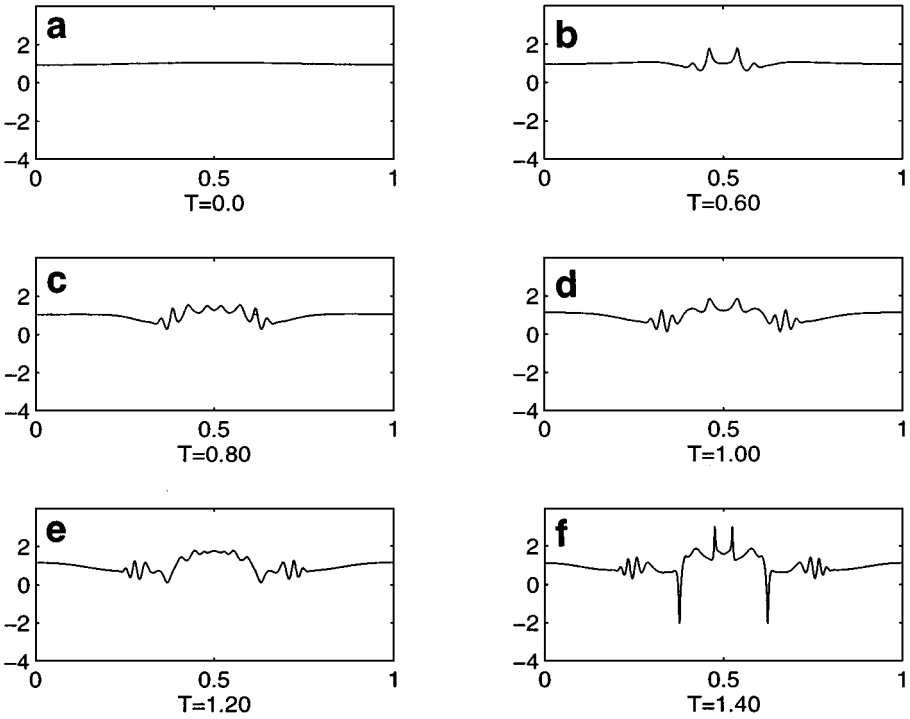

FIG. 10. Inertial vortex sheets, sequence of γ: $S = 0.005$, $N = 1024$, $\Delta t = 1.25 \times 10^{-4}$: (a) $t = 0$; (b) $t = 0.60$; (c) $t = 0.80$; (d) $t = 1.00$; (e) $t = 1.20$; (f)$t = 1.40$.

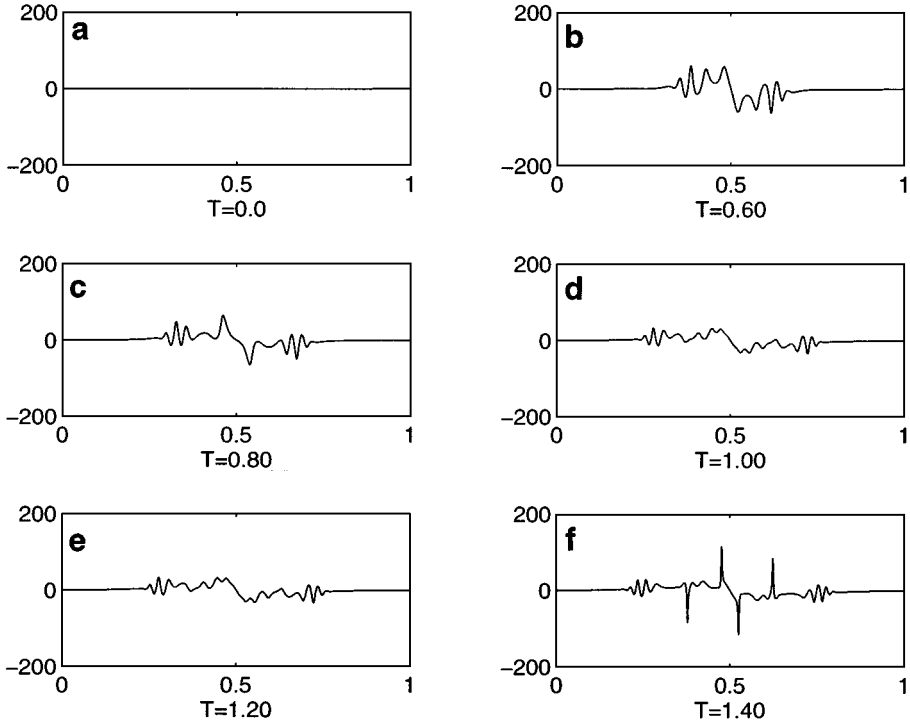

FIG. 11. Inertial vortex sheets, sequence of κ: $S = 0.005$, $N = 1024$, $\Delta t = 1.25 \times 10^{-4}$: (a) $t = 0$; (b) $t = 0.60$; (c) $t = 0.80$; (d) $t = 1.00$; (e) $t = 1.20$; (f) $t = 1.40$.

where T is given by

$$T(\alpha, t) = \int_0^{\alpha} \theta_{\alpha'} U \, d\alpha' - \frac{\alpha}{2\pi} \int_0^{2\pi} \theta_{\alpha'} U \, d\alpha'. \tag{98}$$

By using an implicit discretization like the one we discussed before, we will get a stability constraint of the form

$$\max_{\alpha} |T| \Delta t < C \cdot \frac{L}{2\pi} h. \tag{99}$$

Using the $\kappa - L$ frame, the equations of motion are given by Eqs. (31), (32), and (21), so the stability constraint is of the form

$$\max_{\alpha} |T_1| \Delta t < C \cdot \frac{L}{2\pi} h, \tag{100}$$

where T_1 is given by

$$T_1(\alpha, t) = \frac{L}{2\pi} \int_0^{\alpha} \kappa U \, d\alpha' - \frac{\alpha L}{(2\pi)^2} \int_0^{2\pi} \kappa U \, d\alpha'. \tag{101}$$

Using the relation between θ and κ, $\kappa = \theta_\alpha / s_\alpha$, for here $s_\alpha = L/(2\pi)$, it is easy to see to that $T = T_1$. This shows that the $\kappa - L$ frame and $\theta - L$ frame have the same order stability constraints.

We use this $\kappa - L$ frame because we can apply it to the computation of both 3-D curves and surfaces. The comparison of the results by using the $\kappa - L$ frame and $\theta - L$ frame

shows that our $\kappa - L$ frame shares the same stability property as the $\theta - L$ frame, and yet has the advantage of being applicable to 3-D filaments and surfaces.

7.4. *Motion by Curvature in 3-D*

We now turn our attention to 3-D filaments. First we test our method for the simple motion by curvature in 3-D. We basically confirm the similar performance we observed for the corresponding 2-D problem. We perform a careful comparison with an explicit fourth order Runge–Kutta discretization. For $N = 512$, the maximum allowable time step for our method is 3200 times larger than that for the Runge–Kutta method. We also test the reformulation using the Frènet frame. We found that the computation breaks down at a relative early time due to the formation of a vanishing curvation point. This corresponds to a blowup in the torsion variable. This is an artificial parametrization singularity. The filament is very smooth at this time. Using the generalized curvature κ_1 and κ_2, we can compute well beyond this time without any difficulty.

Consider the 3-D curve

$$\mathbf{X} = (\sin(2\alpha), \cos(\alpha), \sin(\alpha) + 2\cos(2\alpha)), \qquad \alpha \in (0, 2\pi),$$

evolving according to motion by curvature, $\mathbf{X}_t = \kappa\mathbf{N}$. Using our $\kappa_1 - \kappa_2 - \omega - L$ formulation, with $N = 256$ mesh points, and time step $\Delta t = 0.0005$, we show in Fig. 12 the continued evolution of the curve from $t = 0.0$ to $t = 1.4$. We observe that this space curve relaxes to a circle and eventually shrinks to a point.

We compare our method with a straightforward explicit discretization of $\mathbf{X}_t = \kappa\mathbf{N}$ in (x, y, z) coordinates. This involves using a spectral method for the spatial derivatives and fourth order Runge–Kutta method in time. We list below the maximum time step that can be taken to get a stable solution using these two methods. Due to the particle clustering, we can only compute up to $t = 1.0$ using the explicit method. Clearly we can see the huge advantage of using our implicit discretization.

No. of points	Explicit method	$\kappa_1 - \kappa_2 - \omega - L$ method
128	0.000125	0.0750
256	0.00003125	0.0375
512	0.00000625	0.0200

The motion of a 3-D filament by curvature is somewhat different from that of the 2-D counterpart. In the 2-D case, it is possible to interpret the geometrical significance of positive or negative curvature. However, for 3-D curves, the curvature is defined by

$$\kappa = \sqrt{\mathbf{X}_{ss} \cdot \mathbf{X}_{ss}} = |\mathbf{X}_{ss}|. \tag{102}$$

The positive square root is taken in Eq. (102) and thus the curvature is always nonnegative, $\kappa \geq 0$. When it passes through points where $\kappa = 0$, the normal vector $\mathbf{N}$ varies discontinuously. Moreover, at points where $\kappa = 0$, the torsion is not well defined. Recall that the torsion is defined by

$$\tau = \kappa^{-2}(\mathbf{X}_s \cdot \mathbf{X}_{ss} \times \mathbf{X}_{sss}). \tag{103}$$

It is obvious that the torsion is only defined when the curvature does not vanish.

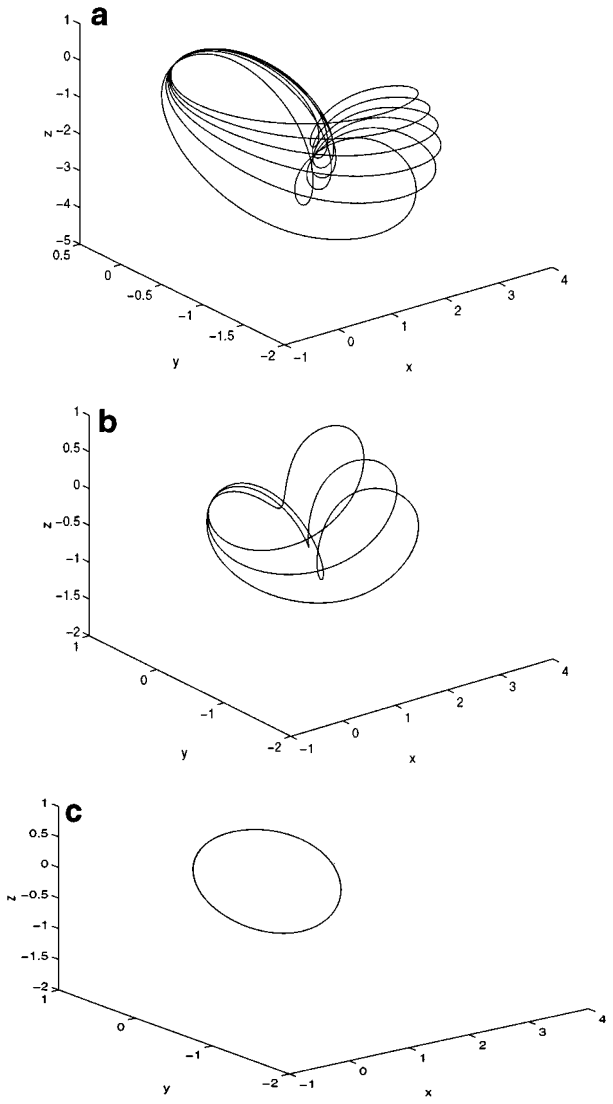

FIG. 12. $N = 256$, $\Delta t = 0.0005$: (a) $t = 0.0, 0.6(0.1)$; (b) $t = 0.7, 1.0(0.1)$; (c) $t = 1.4$.

We tried the same example using $\kappa - \tau - L$ formulation (41), (42), and (43). Numerical difficulties developed around $T = 1.015$ when the curvature became close to zero at some point on the curve. In fact, we were only able to calculate up to $T = 1.015$ using 256 points, no matter how small a time step we took, due to the stability constraints we derived from Eq. (44). On the other hand, we had no difficulty computing past $T = 1.015$ when using the $\kappa_1 - \kappa_2 - \omega - L$ formulation. In Fig. 13, we compare the plots of curvature at $T = 1.015$ using the $\kappa - \tau - L$ formulation and $\kappa_1 - \kappa_2 - \omega - L$ formulation by taking the time step to be $dt = 0.00125$ and $dt = 0.01$, respectively. Here we have used the relationship $\kappa = \sqrt{\kappa_1^2 + \kappa_2^2}$.

We note the similarity in the two plots of the curvature. We also note the jump in the derivative of the curvature as the curvature approaches zero. This means that κ_α is not continuous and that Eqs. (42) and (43) break down.

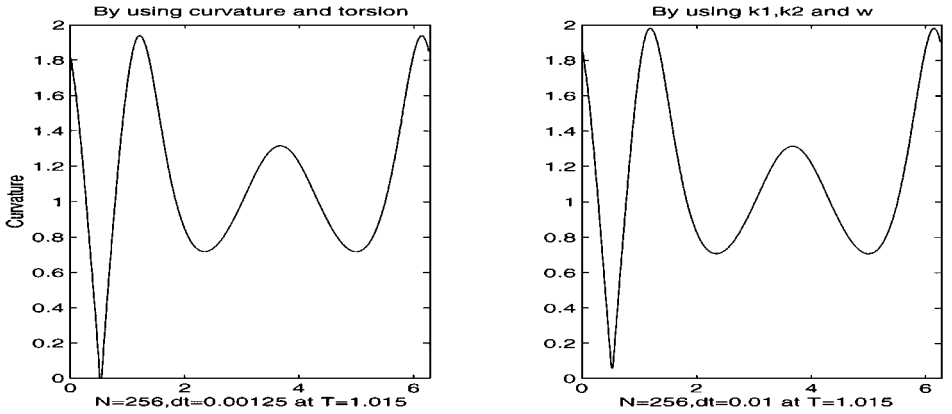

FIG. 13. Comparison of curvature using $\kappa - \tau - L$ and $\kappa_1 - \kappa_2 - \omega - L$ formulation.

We also plot the variables κ_1 and κ_2 at $T = 1.02$ in Fig. 14. Note that these variables remain smooth along the entire curve. Thus we see the advantage and, indeed, necessity of using the $\kappa_1 - \kappa_2 - \omega - L$ formulation instead of the $\kappa - \tau - L$ formulation.

7.5. *Motion of the Kirchhoff Rod Model*

Next we test our numerical methods on the motion of the elastic rods. Two interesting equilibrium states are reached using two different initial perturbation of a circular initial filament. As before, no stiffness is observed using our reformulated implicit schemes. A sequence of snapshots of the dynamics approaching to equilibrium for two examples (radius $r = 1$) are shown in Figs. 15 and 16. In both examples, we choose as initial conditions a circular conformation with total twist $\mathbf{T}\omega = 5$. Here $\mathbf{T}\omega(\mathbf{X}) = \frac{1}{2\pi}\oint \omega(\mathbf{X}(s))\, ds$. In the first example, we choose the initial twist to be distributed uniformly with a small localized perturbation. In particular, we choose $\omega(s, 0) = (5 + \omega_1)/(5 + \frac{1}{2\pi}\oint \omega_1\, ds)$, where

$$\omega_1 = \begin{cases} 0 & |x - \pi| \le \frac{\pi}{2}, \\ \dfrac{1}{4\cosh^2\left(\frac{x-\pi}{2x-\pi}\right)} & \frac{\pi}{2} < x \le \pi, \\ \dfrac{1}{4\cosh^2\left(\frac{\pi-x}{3\pi-2x}\right)} & \pi < x < \frac{3\pi}{2}. \end{cases} \tag{104}$$

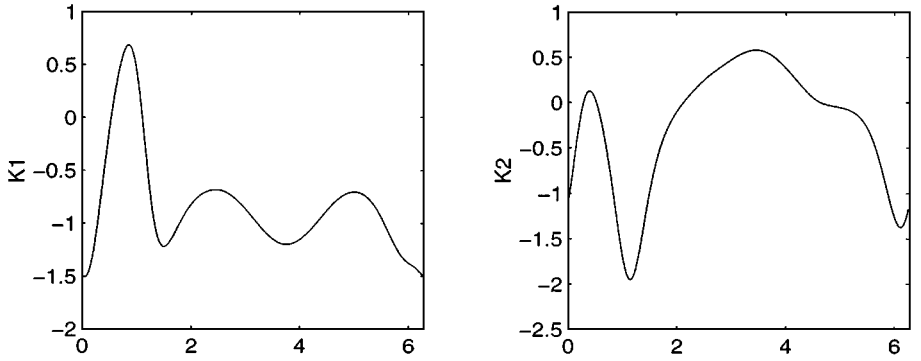

FIG. 14. κ_1 and κ_2 at $T = 1.02$ with $N = 256$ and $dt = 0.01$.

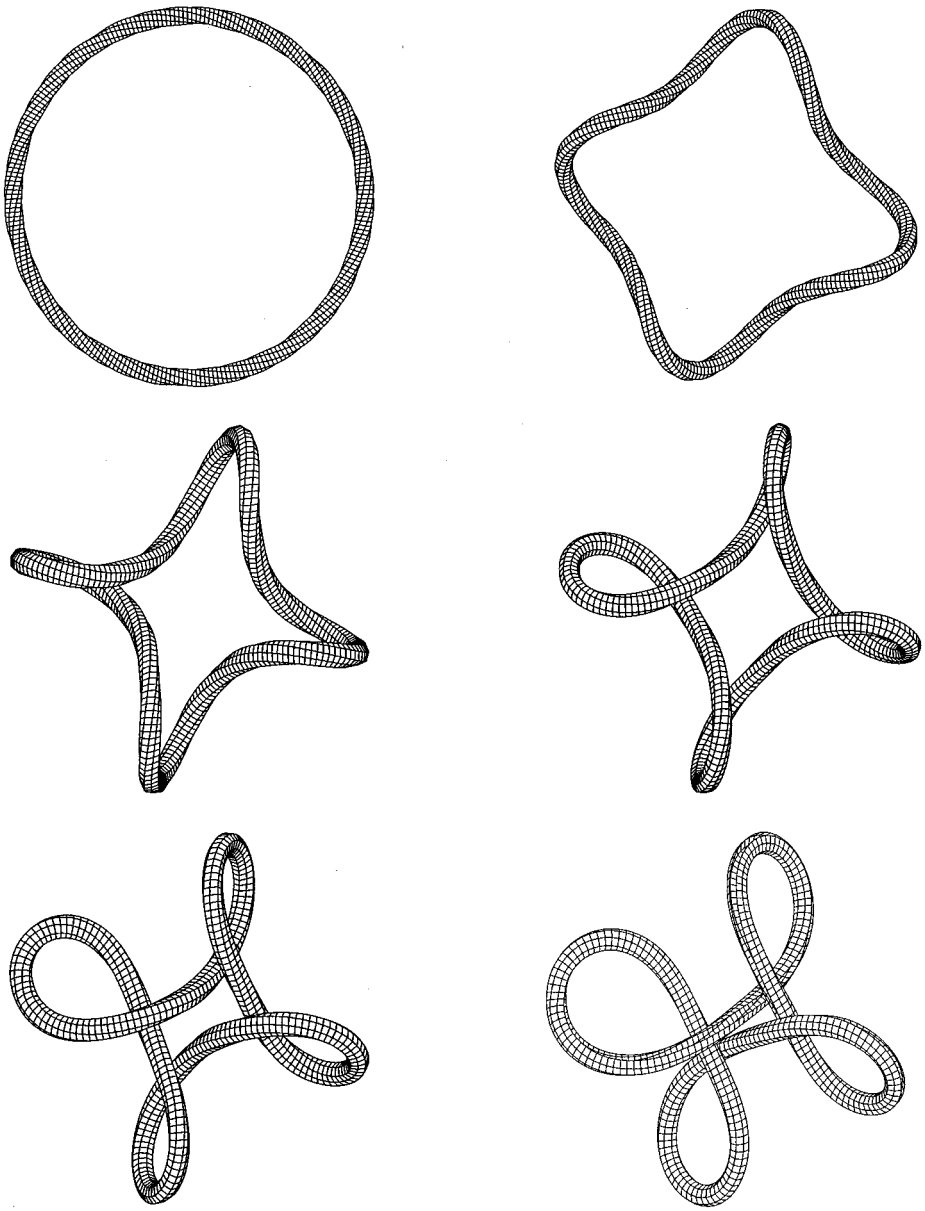

FIG. 15. Approach to equilibrium "clover" configuration. $T = 0, 1.6, 2.1, 2.6, 4, 12$.

In the second example, we use the same parameters and a similar initial condition as the first one, except that the initial twist includes an order one nonlocalized perturbation from uniformity. More precisely, we choose $\omega(s, 0) = 2\pi L^{-1}\mathbf{T}\omega * (1 + 0.8 * \sin(2\pi s/L))$. In both of these examples, we use 256 grid points in our calculations and a time step $dt = 0.00125$. For the first example, the solutions are plotted at $T = 0, 1.6, 2.1, 2.6, 4, 12$, respectively. For the second example, the solutions are plotted at $T = 0, 1.2, 2.4, 2.8, 4, 6, 12$, respectively.

In these two examples, the rods start twisting around $T = 1.6$ and $T = 1.2$, respectively. Because of the contact force, the rods cannot self-cross, and thus they would keep twisting

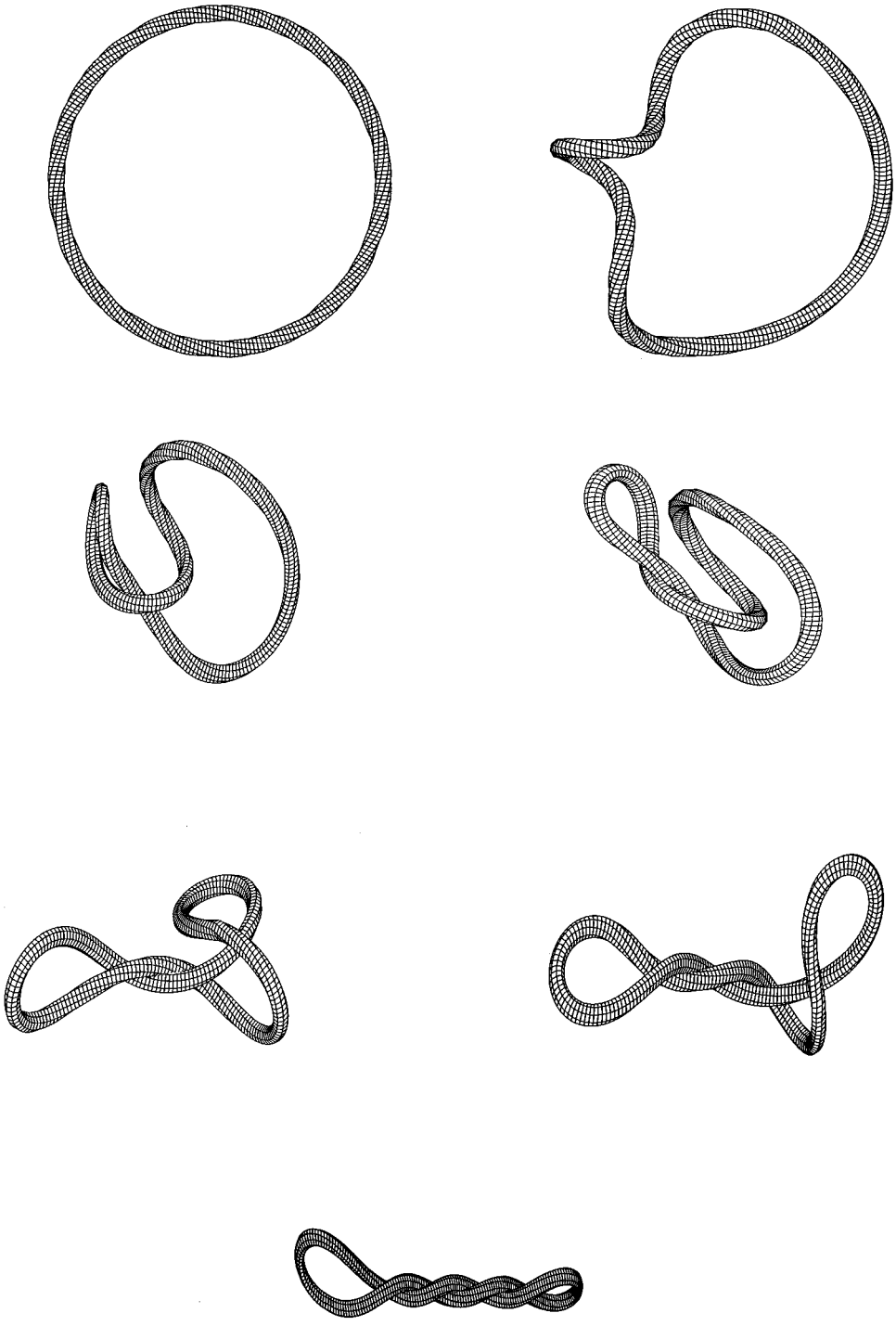

FIG. 16. Approach to equilibrium "plectonemic" configuration. $T = 0$, 1.2, 2.4, 2.8, 4, 6, 12.

until they approach the equilibrium configurations. We have also investigated using different values for the parameters η_1, η_2 in Eqs. (65) and (66). We find that there is little change in the equilibrium states in both examples, but the rate at which the rods evolve to these states is affected.

We should mention the construction of the initial condition for these two examples. In our methods, it is necessary to specify initial values of κ_1, κ_2, and ω. The twist of the circle ω is already given, so we need to determine κ_1 and κ_2 from the curvature κ and the torsion τ. Since $\kappa_1^2 + \kappa_2^2 = \kappa^2$, we parameterize κ_1, κ_2 by κ and ϕ as

$$\begin{aligned} \kappa_1 &= \kappa \cos\phi \\ \kappa_2 &= \kappa \sin\phi. \end{aligned} \tag{105}$$

Note that the torsion τ is zero everywhere for an unit circle. Substituting the above equations into Eq. (47), we get

$$\phi_s = \omega.$$

Thus we are able to calculate ϕ. The curvature of the unit circle is 1. Thus κ_1 and κ_2 are completely determined by Eq. (105).

Finally, it is necessary to include some sort of contact force $g(s)$ to prevent the elastic rod from self-crossing. In a similar way to [10] we have set

$$g(s) = -\int M(r(s), r(\sigma)) \frac{r(s) - r(\sigma)}{(|r(s) - r(\sigma)|)^{10}}\, d\sigma. \tag{106}$$

The purpose of the mollifier M is threefold. First, some distinction must be made between nearest neighbor points along the curve and other points that are far away in arc length but are close in space. Clearly, for those points which are nearest neighbors along the curve, no contact force is necessary and therefore M is set to be zero. However, if two points which are separated by a large distance in arc length become close to each other in space, M must be nonzero to activate the contact force. Therefore, M helps prevent self-crossing while ensuring that points along the curve are not forced apart.

Second, the magnitude of the contact force needs to be controlled to prevent overly large forces from destabilizing our solution. The contact force has the form of a stiff inverse power law ($\propto r^{-10}$) so some care must be taken in choosing a constant of proportionality. This is the other role that M plays when the contact force is in effect. We assume the radius of the rod is approximately 3 times the grid spacing, i.e., hs_α, and thus M needs to be chosen so that the distance between any two points which are not close in arc length cannot be smaller than $6hs_\alpha$. We do not have an explicit expression for M here. In our first example, we simply take M to be 0.005 if the distance is less than $12hs_\alpha$ but greater than $8hs_\alpha$, and 0.1 if the distance is less than $8hs_\alpha$. In our calculation $s_\alpha = L/2\pi$ is very close to 1. In our second example, we take M to be 0.004 if the distance is less than $14hs_\alpha$ but greater than $8hs_\alpha$, and 0.04 if the distance is less than $8hs_\alpha$.

Third, by setting $M = 0$ when $r(s)$ and $r(\sigma)$ are distant we reduce the computational cost in evaluating (106) from what would be $O(n^2)$ to $O(n)$. This step is absolutely necessary in order to prevent the evaluation of $g(s)$ from dominating the entire computation.

By way of comparison, Ref. [10] used a similar model to calculate the evolution of an elastic rod. The method there was to directly discretize Eqs. (65)–(67) using second order centered differences. Here we have the considerable advantage that no high order

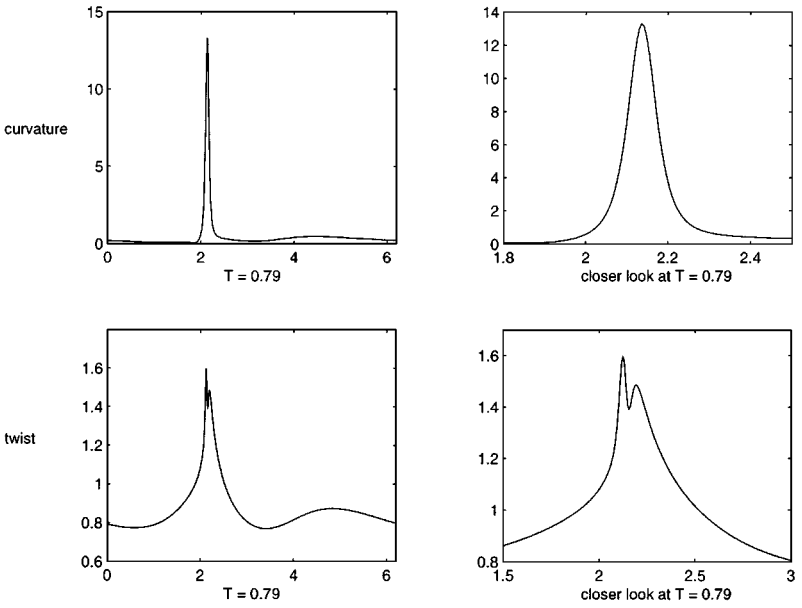

FIG. 17. Curvature and twist of the second filament at $t = 0.79$.

time step stability constraints are imposed. This advantage is crucial if accurate, long-time computations (such as DNA modelling) are to be attempted.

It is interesting that both of these examples start from unit circles with the same total twist. The only difference is the distribution of the initial twist. But they approach totally different equilibrium states. The clover-like structures are also observed in Langevin dynamics simulations [15] and the plectonemic conformation is similar to DNA studies.

7.6. *Motion of Anti-parallel Pair of Vortex Filaments*

Finally, we are going to test our method on the motion of anti-parallel vortex filaments. We consider large amplitude antisymmetric helical initial perturbations of anti-parallel pair [4, 13]:

$$\mathbf{X}_1 = (-0.5 + 0.3\cos\alpha, 0.3\sin\alpha, \alpha) \tag{107}$$

$$\mathbf{X}_2 = (0.5 + 0.3\cos\alpha, 0.3\sin\alpha, \alpha) \qquad \alpha \in (0, 2\pi). \tag{108}$$

The circulation strengths Γ_1, Γ_2 in Eq. (81) are taken to be 1 and -1, respectively. We apply the fourth order implicit–explicit scheme in our numerical experiments and find that the time step is indeed linearly dependent on the spacial mesh size as we expected. However, the fourth order scheme for this particular problem requires a small time step for stability constraint. Instead, we use the second order implicit–explicit scheme in our computation. The second order implicit–explicit scheme (see subsection 6.1) simply uses the leap frog scheme for the lower order term and the implicit Crank–Nicolson scheme for the leading order term:

$$\frac{1}{2\Delta t}(u^{n+1} - u^{n-1}) = f(u^n) + \frac{\nu}{2}[g(u^{n+1}) + g(u^{n-1})]. \tag{109}$$

Snapshots of the evolving filaments at times $t = 0$, 0.73 and 0.79 are given in Figs. 18–20

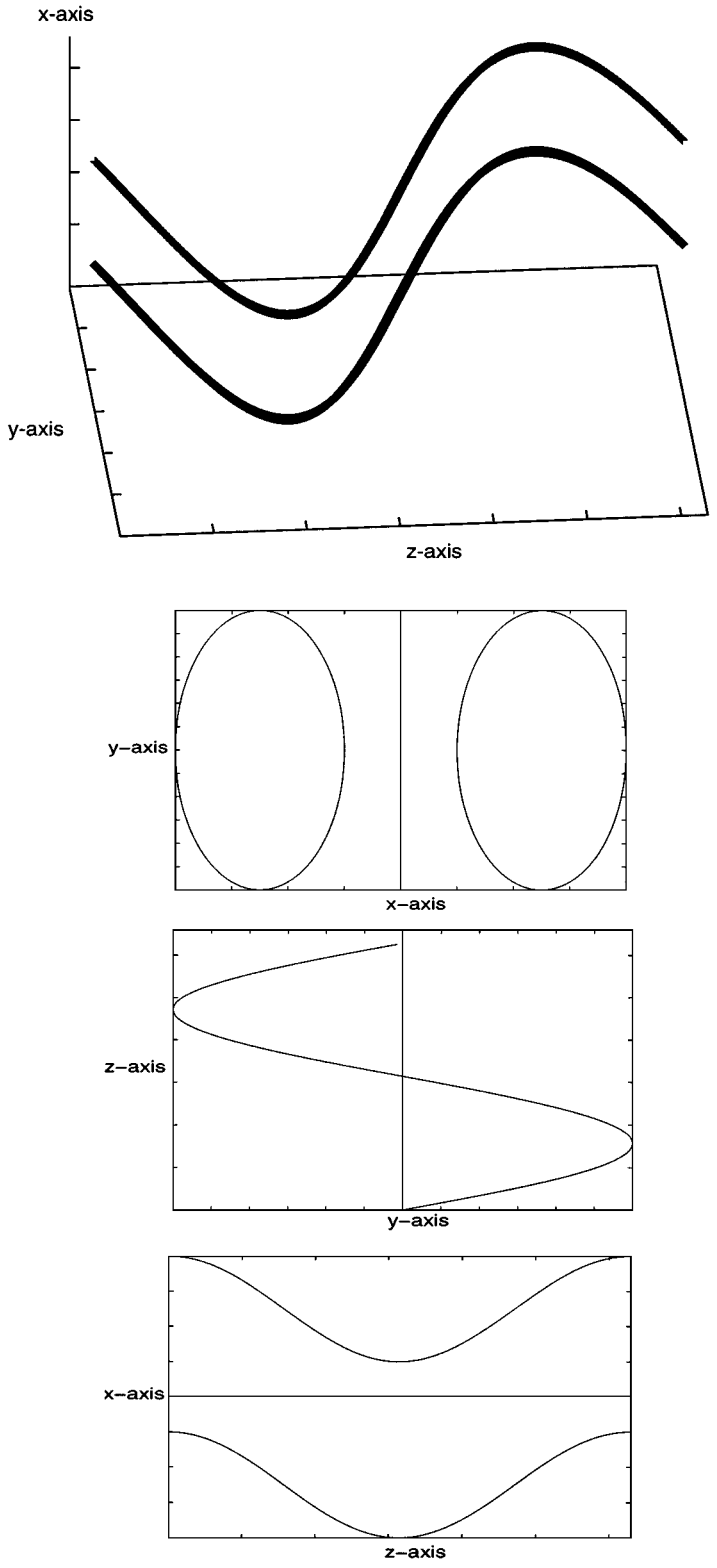

FIG. 18. Snapshot of filaments for antisymmetric perturbation at $t = 0$.

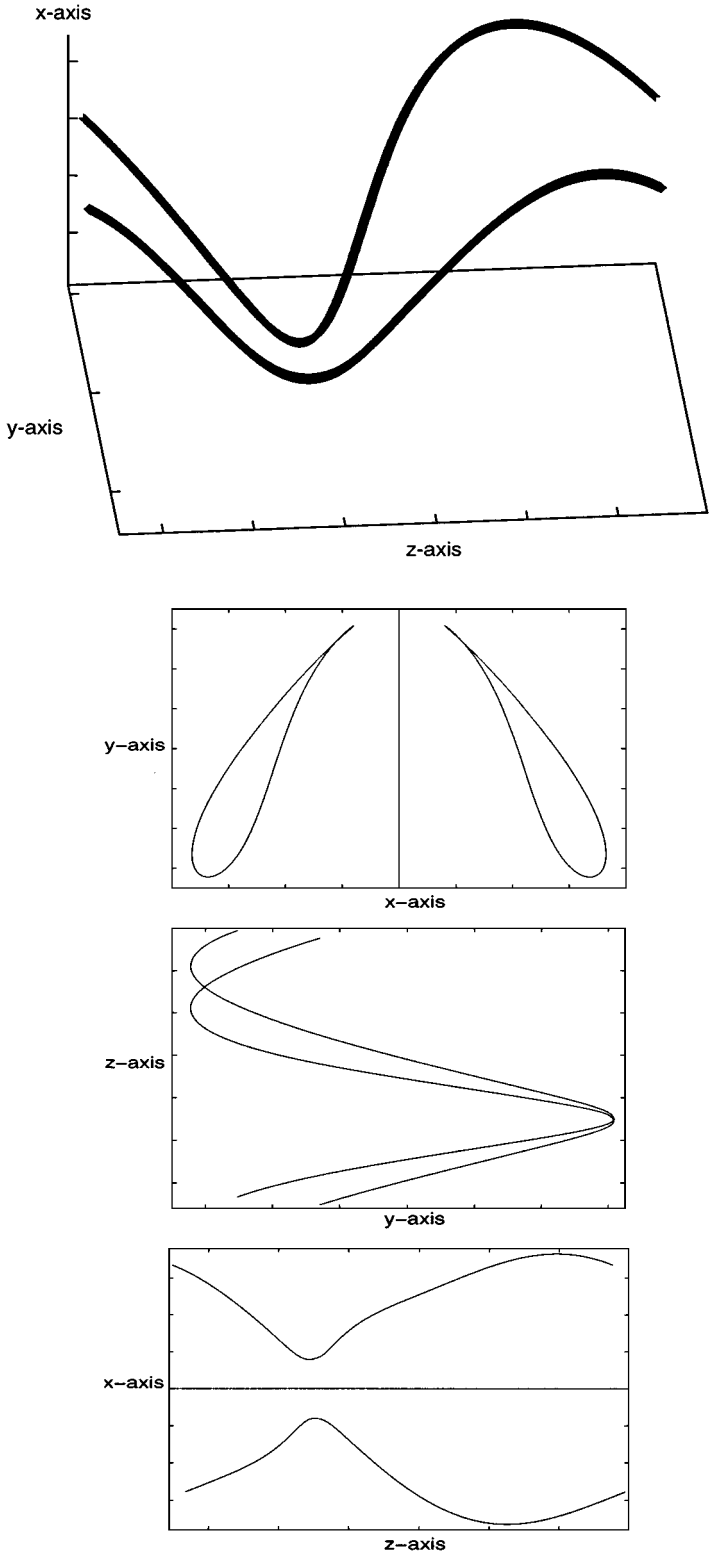

FIG. 19. Snapshot of filaments for antisymmetric perturbation at $t = 0.73$.

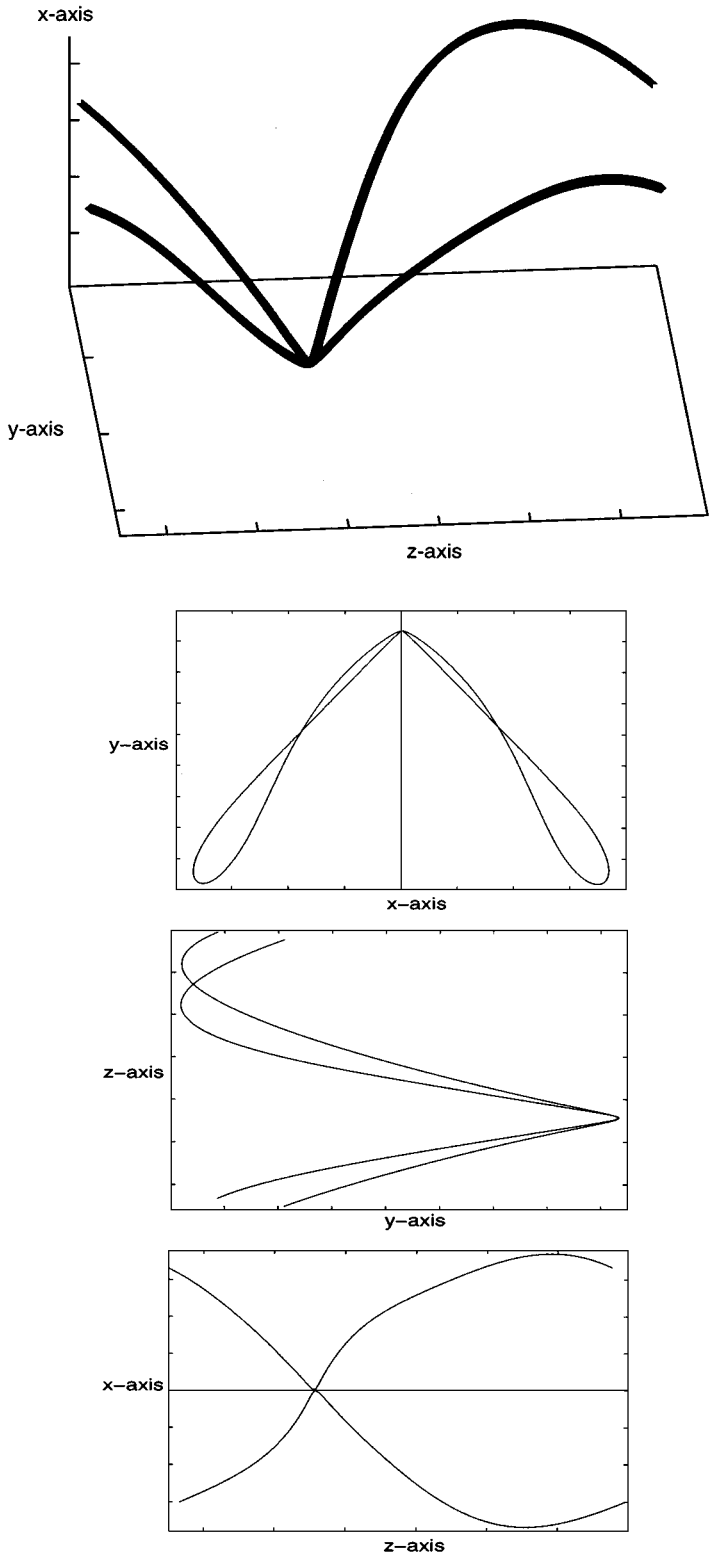

FIG. 20. Snapshot of filaments for antisymmetric perturbation at $t = 0.79$.

where 1024 mesh points and time step $\Delta t = 0.00125$ are used. The initial separation distance between the two filaments is constant, and as time evolves, the minimum separation distance decreases until the pair collapses around $t = 0.79$. In Fig. 17, we also show the curvature κ and the twist ω of the second filament $\mathbf{X}_2$ at time $t = 0.79$. Using our method, we are also able to include the other nonlocal effects that are neglected in the simplified equations (81).

8. SUMMARY

A new formulation and new methods are presented for computing the motion of a curvature driven 3-D filament. These numerical methods have no high order time step stability constraints. Our methods are applied to compute the motion of 2-D vortex sheets with surface tension, motion of 3-D filament by curvature, the Kirchhoff rod model and anti-parallel vortex filaments. Our numerical results demonstrate convincingly that our method removes the severe time step stability constraint associated with explicit discretizations for both 2-D and 3-D curves. It shares a stability property and computational efficiency similar to those of the $\theta - L$ formulation derived by Hou *et al*. in [7] for 2-D interfaces. There are many interesting physical and biological applications of motion of 3-D curvature-driven filaments. Our method provides an effective numerical technique for studying these problems. This technique can also be extended to compute 3-D free surfaces. This will be the topic of a future paper.

REFERENCES

1. U. M. Ascher, S. J. Ruuth, and B. Wetton, *SIAM J. Numer. Anal*. **32**, 797 (1995).
2. G. Baker, D. Meiron, and S. Orszag, *J. Fluid Mech.* **123**, 477 (1982).
3. A. J. Callegari and L. Ting, *SIAM J. Appl. Math*. **35**, 148 (1978).
4. S. Crow, *AIAA J*. **8**, 2172 (1970).
5. D. A. Kessler, J. Koplik, and H. Levine, *Phys. Rev. A* **30**, 3161 (1984).
6. E. H. Dill, *Arch. Hist. Exact* **44**, 1 (1992).
7. T. Y. Hou, J. S. Lowengrub, and M. J. Shelley, *J. Comput. Phys*. **114**, 312 (1994).
8. J. P. Keener and J. J. Tyson, *SIAM Rev.* **34**, 1 (1992).
9. G. Kirchhoff, *Mechanik* **28** (1876).
10. I. Klapper, *J. Comput. Phys*. **125**, 325 (1996).
11. I. Klapper and M. Tabor, *J. Phys. A* **27**, 4919 (1994).
12. R. Klein and A. Majda, *Physica D* **49**, 323 (1991a).
13. R. Klein, A. J. Majda, and K. Damodaran, *J. Fluid Mech*. **288**, 201 (1995).
14. D. W. Longcope and I. Klapper, *Astrophys. J*. **488**, 443 (1997).
15. G. Ramachandran and T. Schlick, *Beyond Optimization: Simulating the Dynamics of Supercoiled DNA by a Macroscopic Model, DIMACS Series in Discrete Mathematics and Theoretical Computer Science*, edited by P. Pardalos, D. Shalloway, and G. Xue (Am. Math. Soc., Providence, RI, 1995).
16. P. G. Saffman and G. R. Baker, *Annu. Rev. Fluid. Mech.* **11**, 95 (1979).
17. T. Schlick, *Curr. Opin. Struct. Biol*. **5**, 245 (1995).
18. J. J. Tyson and S. H. Strogatz, *Int. J. Bifur. Chaos* **1**, 723 (1991).
19. E. E. Zajac, *J. Appl. Mech.* **29**, 136 (1962).